Huang *et al. Earth, Planets and Space* *(2025) 77:10*
https://doi.org/10.1186/s40623-025-02135-7

Earth, Planets and Space

FULL PAPER **Open Access**

Complexity of near-surface deformation and subsurface structure of the Chihshang creeping fault-line scarp, eastern Taiwan: insights from integration of geological and geophysical data

W. J. Huang[1,2*], M. T. Fitrianto[1], C. C. Chen[2,3], P. Y. Chang[2,3], I. C. Yen[1,4], M. Le Béon[1,3] and S. T. Lu[5]

Abstract

The precise position and geometry of a fault and the recognition of contemporary active strands are pivotal elements for formulating regulations for earthquake fault zones and fault setbacks. The western frontal escarpment toe of the Coastal Range in Tapo, eastern Taiwan is commonly considered as the plausible location of the N18°E-trending, east-dipping Chihshang creeping seismogenic fault. Frontal collapse and flattening of reverse faulting, in addition to fluviation and landslide have complicated the process for defining the Chihshang fault configuration. We used a multidisciplinary approach, combining site investigation, geological core analysis and correlation, resistivity prospecting, and inclinometer monitoring, to illuminate the subsurface structure and deformation of the leading edge of the Chihshang fault at Tapo Elementary School. We found that (1) the Chihshang main fault is a contact of alluvium deposits and the mudstone of Lichi mélange, and has a dip angle of approximately 77° within the resistivity gradation zone 55 m east of the toe of the geomorphic escarpment; (2) it has a 2-year cumulative horizontal displacement of 20.7 mm northwestward and continuously creeps without seasonal variation; and (3) the active deformation on the escarpment results from a combined effect of fault creeping and slow gravity sliding of the mass which is steadily supplied by the Chihshang reserve faulting. A mechanism of faulting-relay landsliding is proposed to understand the active deformation on the escarpment. Great caution is needed in the interpretation of the aseismic surface ruptures along the inferred trace of reverse creeping faults as fault branching.

Highlights

- The Chihshang fault with a dip angle of 77° is located 55 m east of the escarpment toe, which was once thought to be fault trace in Tapo.
- The fault has a left-lateral slip rate of 8.2 mm/year and a transverse slip rate of 6.4 mm/year and continuously creeps without seasonal variation.
- A mechanism of faulting-relay landsliding is proposed to interpret the active deformation on the escarpment at Tapo Elementary School.

---

*Correspondence:
W. J. Huang
huang22@ncu.edu.tw
Full list of author information is available at the end of the article

Keywords Active fault, Chihshang fault, Longitudinal valley fault, Escarpment, Landslide

Graphical Abstract

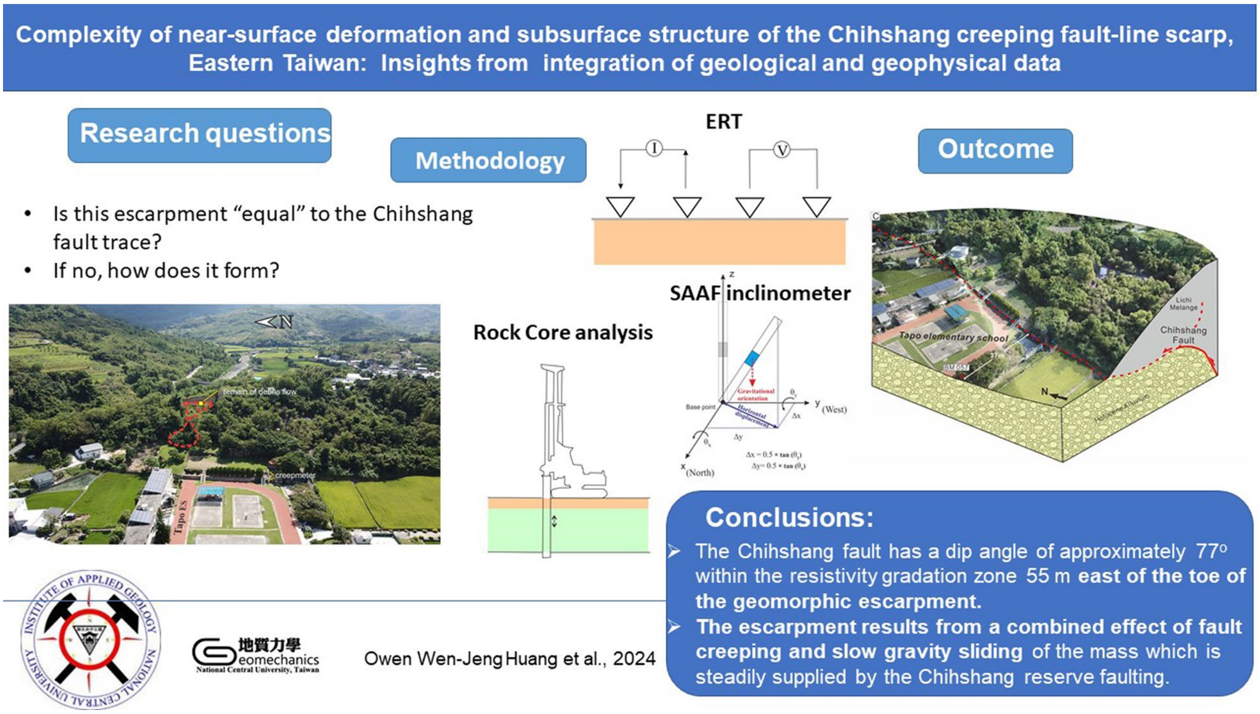

Complexity of near-surface deformation and subsurface structure of the Chihshang creeping fault-line scarp, Eastern Taiwan: Insights from integration of geological and geophysical data

Research questions

- Is this escarpment “equal” to the Chihshang fault trace?
- If no, how does it form?

Methodology

ERT

Rock Core analysis

SAAF inclinometer

Outcome

Conclusions:

- The Chihshang fault has a dip angle of approximately 77° within the resistivity gradation zone 55 m **east of the toe of the geomorphic escarpment.**
- **The escarpment results from a combined effect of fault creeping and slow gravity sliding** of the mass which is steadily supplied by the Chihshang reserve faulting.

Owen Wen-Jeng Huang et al., 2024

1 Introduction

Deformation zones induced by co-seismic faulting can lead to severe damage to buildings and facilities within (e.g., Lawson 1908; Reid 1910; Steinbrugge et al. 1973; Lazarte et al. 1994; Johnson et al. 2002; Yang and Mavroeidis 2018). Almost no structure can sustain deformation if located on the causal fault (Konagai 2005). The vulnerability of engineering structures crossing active faults has been studied after two devastating earthquakes in 1999, i.e., the Mw 7.4 İzmit earthquake in Turkey and Mw 7.6 Chi-Chi earthquake in Taiwan (e.g., Bird and Bommer 2004; Faccioli et al. 2008; Pamuk et al. 2005). It has been demonstrated that fault location, fault angle, and sense and magnitude of fault slip are the main factors affecting the characteristics of deformation zones (e.g., Huang and Johnson 2010; Chang et al. 2015). In recent years, numerical simulation based on not only continuum analysis (Anastasopoulos and Gazetas 2007; Agalianos et al. 2019; Fadaee et al. 2020), but also particle-based analysis (Garcia and Bray 2019a, 2019b; Li et al. 2019; Liu et al. 2020; Lin et al. 2021) has been demonstrated as a reliable tool for studying the mechanical behavior of the fault–soil–structure systems. No matter how powerful the numerical simulation methods are, the geometric features and behavior of fault ruptures remain crucial inputs nevertheless for the analysis of fault–structure interactions (Lin et al. 2021). However, the frontal collapse and flattening of reverse faulting with fluviation and landslide make it hard to map the active fault trace, i.e., the precise position and geometry of the fault, or identify contemporary active strands (Fairbridge 1968).

The Chihshang fault (hereinafter referred to as ChF) in eastern Taiwan is one of the most active segments of the Longitudinal Valley Fault (LVF) (Chen et al. 2007) and generally considered as the suture of Eurasian and Philippine Sea plates (Chai 1972; Biq 1972; Wu 1978; Angelier et al. 1986; Ho 1986). Previous studies (Yu et al. 1994; Angelier et al. 1997, 2000; Lee et al. 2003, 2006; Mu et al. 2011) have shown that the ChF has two types of movement: co-seismic stick–slip motion and inter-seismic aseismic slip. The co-seismic movement corresponded to the 1951 Chihshang Earthquake (Mw = 6.2) (Cheng et al. 1996), the 1992 Chengkung

Earthquake ($M_L = 5.4$) (Yu et al. 1994; Shin and Chang 1992) and the 2003 Chengkung Earthquake (Mw = 6.5) (Chen et al. 2006; Wu et al. 2006; Hu et al. 2007). The inter-seismic movement, which is aseismic creeping, was revealed in a series of studies on the direct monitoring of slow faulting in man-made structures (Angelier et al. 1997, 2000; Lee et al. 2000, 2001; Mu et al. 2011). The western frontal geomorphic escarpment of the Coastal Range has been commonly regarded as a fault scarp, explicitly meaning the surface trace of the ChF in numerous places for decades including at our study site at Tapo Elementary School (hereafter referred to as Tapo ES). The ongoing frontal deformation at Tapo ES has been considered to be related to faulting but with caution due to local topographic effects and gravity sliding (Angelier et al. 2000; Lee et al. 2003; Chang et al. 2003). In recent years, Chang et al. (2018) suggested that the actual fault plane in Tapo is on the hillside tens of meters away from the toe of the topographic escarpment on the basis of resistivity images and should be further to the east of the boreholes that they had drilled. In fact, they did not truly find the fault plane and their electric resistivity tomography (ERT) has no capacity to decipher the geometry of the ChF without further verification. Thus, the geometry of subsurface structures remains unclear, which is important for the mitigation of earthquake hazards. Moreover, the mechanism of the frontal deformation deserves further exploration.

In this study, we utilized several methods to reconstruct the geometry of the ChF and understand the mechanism of surface creeping at Tapo ES, as well as how the fault slip is transferred from the depths to the earth's surface. Specifically, we utilized coring and detailed core descriptions of the footwall, hanging wall, and the fault zone, as well as C^{14} dating of key horizons, and downhole inclinometer monitoring. These data were then integrated with two 2-D electric resistivity tomography surveys and cross-hole lithologic correlations. This study has a twofold purpose: (1) to construct the subsurface structures beneath the fault-line scarp, particularly to attain quantitative data of the ChF at this site, as one classic type of frontal deformation of reverse faults and (2) to derive how the fault-line scarp evolved, including its current creeping mechanisms. This study shows three unpublished boreholes which all penetrate through the ChF at different depths and a novel result from an inclinometer monitoring the mobility of the ChF. Unlike Chang et al. (2018) and other studies (e.g., Angelier et al. 2000; Lee et al. 2006), the ChF angle are found up to 77° at the depth greater than 20 m and its trace is 55 m away from the slope toe. Unlike Lee et al. (2003), the result of our inclinometer data shows the ChF continuously creeps without seasonal variation. Unlike Chang et al. (2018) suggested that the frontal deformation of the escarpment resulted from the sudden mass movement induced by the inter-seismic creeping, we show the active deformation on the escarpment results from a combined effect of fault creeping and slow gravity sliding of the mass which is steadily supplied by the Chihshang faulting. Our results are helpful for refining reverse earthquake fault zones, assessing earthquake hazard, and understanding fault creep.

2 Background and tectonic setting

An earthquake sequence with three major earthquakes of local magnitudes larger than 7.0 occurred in eastern Taiwan in 1951 (Shyu et al. 2006), corresponding to the development of three surface ruptures associated with the Milun Fault, Yuli Fault, and ChF from north to south in the Hualien-Taitung Longitudinal Valley (Fig. 1a) (Hsu 1962; Shyu et al. 2006). The ChF with a length of approximately 35 km is located in the middle of the southern half of the Longitudinal Valley and classified as an active fault of the first category by the Taiwan Central Geological Survey (Lin et al. 2000); that is, this fault has been active in the past ten thousand years. Its geometry at depth has been inferred from relocated seismicity (e.g., Chen and Rau 2002; Kim et al. 2005; Wu et al. 2006), which shows that the fault dips to the east and has a listric shape with variable dip angle decreasing from 60° at a depth of 5 km to 20° at a depth of 20 km. It belongs to the long-lineament major fault that traverses approximately 150 km from Hualien to Taitung (Fig. 1a). This long lineament is the LVF, which separates the Central Range (deformed China continental margin) to the west and the Coastal Range (the northern segment of the Luzon Arc) to the east (Fig. 1a). The Central Range is composed of pre-Cenozoic continental basement unconformably overlain by metamorphosed Eocene to Miocene clastics (Lin et al. 2003), while the Coastal Range is composed of Miocene accreted volcanic arc, Plio-Pleistocene deep-sea deposits, and mélange (Teng 1987; Chen and Wang 1988; Chen 1997). The LVF is one of the most active faults, accounting for approximately 30% of the 40,000 earthquakes that occur annually in Taiwan (Chen et al. 2007). It exhibits both seismic and aseismic slip, with a slip rate of up to 50 mm/year (Thomas et al. 2014). Such high tectonic activity along the LVF results from the tectonic setting of Taiwan. The LVF represents the suture of the Eurasian Plate and the Philippine Sea Plate, with relative convergence at a rate of about 82 mm/year at 310° (Yu et al. 1997; Yu and Kuo 1999). Such fast collision rate has also resulted in 17 large, $M \geq 7.0$, disastrous earthquakes in and near Taiwan Island since 1683 (Tsai 1985; Lin et al. 2000; Ng

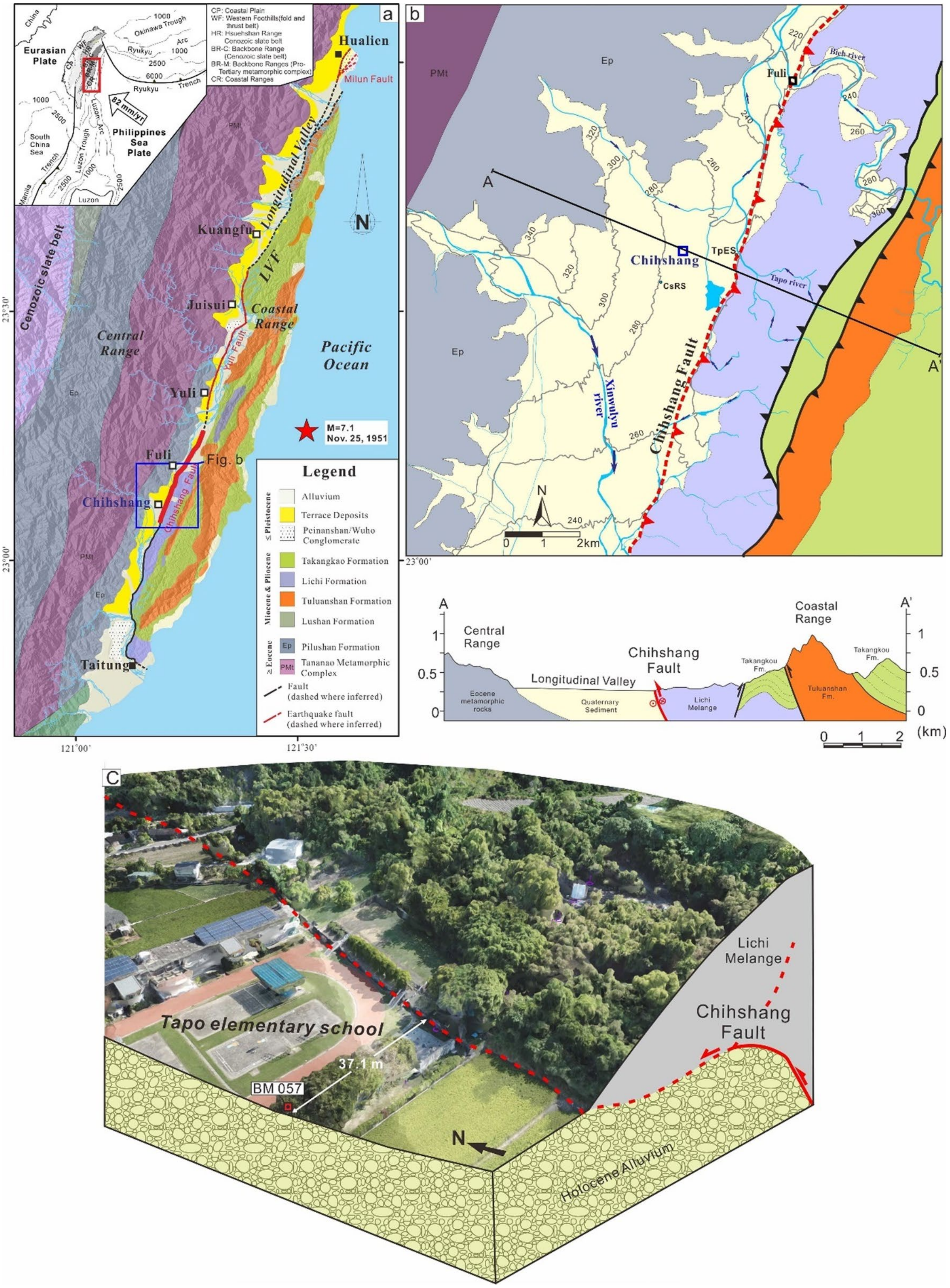

Fig. 1 Geologic setting of ChF at different scales **a**. Regional scale (modified from Taiwan Central Geological Survey 2000). There were two earthquakes with a magnitude of larger than 7, occurring on Oct. 22 and Nov. 25, 1951. The locations of their epicenters are 23°54′N, 121°42′E (out of range) and 23°12′N, 121°30′E (red star on the map). **b** Local scale. TpES and CsRS denote Tapo ES and Chihshang rainfall station, respectively. **c** Site scale. The coordinates of BM057 are 23°07′30.0"N 121°13′50.0"E provided by Yu, Shui-Beih and Chen, Horng-Yue, Academia Sinica in Taiwan. BM is an abbreviation for benchmark

et al. 2009). Various geodetic measurements have indicated that the southern segment of the LVF has a characteristic of aseismic creep, based on repeated survey data of trilateration networks and leveling routes (Yu and Liu 1989), repeated GPS data (Yu and Kuo 2001), and PALSAR (Phased Array type L-band Synthetic Aperture Radar) images provided by the ALOS satellite (Champenois et al. 2012). Such observations have suggested that the ChF creeps entirely along its surface trace. This common aseismic creep of the ChF has been considered an effect of the mudstone of the Lichi M Mélange (Lee et al. 2008) or more specifically the microscopic structure of the gouge in the Lichi Mélange (Thomas et al. 2014). In addition, amorphous materials as fault lubricant were discovered in the creeping zone of the ChF (Wu et al. 2020; Rowe et al. 2019).

The ChF trends N18°E with a horizontal transverse component of nearly 17 mm/year and a left-lateral component of nearly 14 mm/year (Angelier et al. 2000). The trace of the ChF is largely considered to follow a geological contact between the Pliocene Lichi Mélange to the east and Quaternary deposits to the west. The Lichi mélange is composed of Pliocene marine clays (Fig. 1), mixed with a variety of exotic blocks, including ophiolitic rocks and Miocene sandstones in the hanging wall of the ChF (Chang et al. 2000). The footwall is covered with thick Pleistocene–Holocene alluvial sediments (Angelier et al. 2000). In fact, it is difficult to accurately locate the fault trace in the field owing to dense vegetation and agriculture in the region that either covers or blurs the contact. For this reason, the geomorphic scarp bounding the eastern side of the Longitudinal Valley is commonly regarded as the first-order location for the trace of the ChF (Figs. 1c and 2a). Furthermore, Yu and Liu (1989) reported evidence of vertical active creep of the ChF based on leveling data from 1987 to 1989 (Fig. 2a and c). The results of those leveling surveys were consistent with the major geomorphic scarp near Chihshang Township. A significant uplift rate, of ~ 19 mm/year, was observed between two benchmarks 96 m apart (i.e., a projected distance in the direction perpendicular to the fault trace), located on either side of the scarp in Tapo. This uplifting is also consistent with more recent geodetic data from 2007 to 2015 (Hsu et al. 2018), showing that the western margin of the Coastal Range, east of the geomorphic scarp, is uplifted at ~ 20 mm/year with respect to the Longitudinal Valley, west of the geomorphic scarp. Thus, this geomorphic scarp has been inferred as the fault scarp that was generated due to the ChF activity. Correspondingly, a cluster of up to six moderate earthquakes (M 6–7) occurring in the past 800 years was reported by Yen et al. (2014) based on a series of ChF paleoseismic trenches excavated on the toe of the geomorphic scarp. During one of those events, among the 1951 Taitung earthquakes, several fractures were generated in the ground and buildings along the trace of the ChF (Shyu et al. 2006). Furthermore, during the inter-seismic period, fractures continued to develop in concrete water channels, retaining walls, houses, etc., along the ChF zone (Angelier et al. 1997, 2000).

The distinct geomorphic feature is the sudden topographic relief between the hill and the Longitudinal Valley where the Tapo River emerges abruptly into a flat plain (Figs. 1c and 3). In this study, we defined the westernmost side of the hill as the frontal slope, which has a height of 25 m in Tapo. Note that there is a roughly 1.5-m-high escarpment at its toe in the Tapo ES area (Fig. 3). The evidence of ground deformation can be observed clearly, especially along this escarpment. At Tapo ES, the escarpment has been covered by a concrete retaining wall for more than two decades. Thus, the occurrences of ground deformation were detected by the damage to the concrete wall. Damage was noticed along the southern part of the retaining wall (Fig. 3b) during our field observation in late 2018. The upper-half of this concrete wall was pushed out. We also noticed that some man-made metal structures had been built to support the wall and apparently to prevent further damage. Such a phenomenon indicated the horizontal or, say, downward movement of the slope mass. There was a garden slide built to straddle the escarpment above the pushed-out-wall. The platform of the slide was on top of the escarpment, while the toe of the slide was on the ground as low as the toe of the escarpment. The platform of the garden slide was tilted upward towards the west (Fig. 3b). The rotation of this platform indicated frontal deformation on the escarpment, which quantitatively confirmed by creepmeters installed next to the slide, with shortening of ~ 16.2 mm/year (Lee et al. 2003; Fig. 3a). There was also damage on the northern part of the retaining wall (Fig. 3c), which was tilted and fitted with another man-made metal structure to prevent further damage. The middle part of the retaining wall, between these two damaged sites, was renewed in May 1997. In late 2018, the wall appeared convexly outward without any break. However, the platform of the other slide straddling the wall seemed to be detached from the upper base of the slide with emergent fractures. Other evidence of ground deformation was observed on the slope of the hill. The part of the slope abutting to the school was shaped into three stages and became a recreation area (Fig. 3a). Each of the stages was bounded by a concrete retaining wall trending as the escarpment. The third retaining wall from

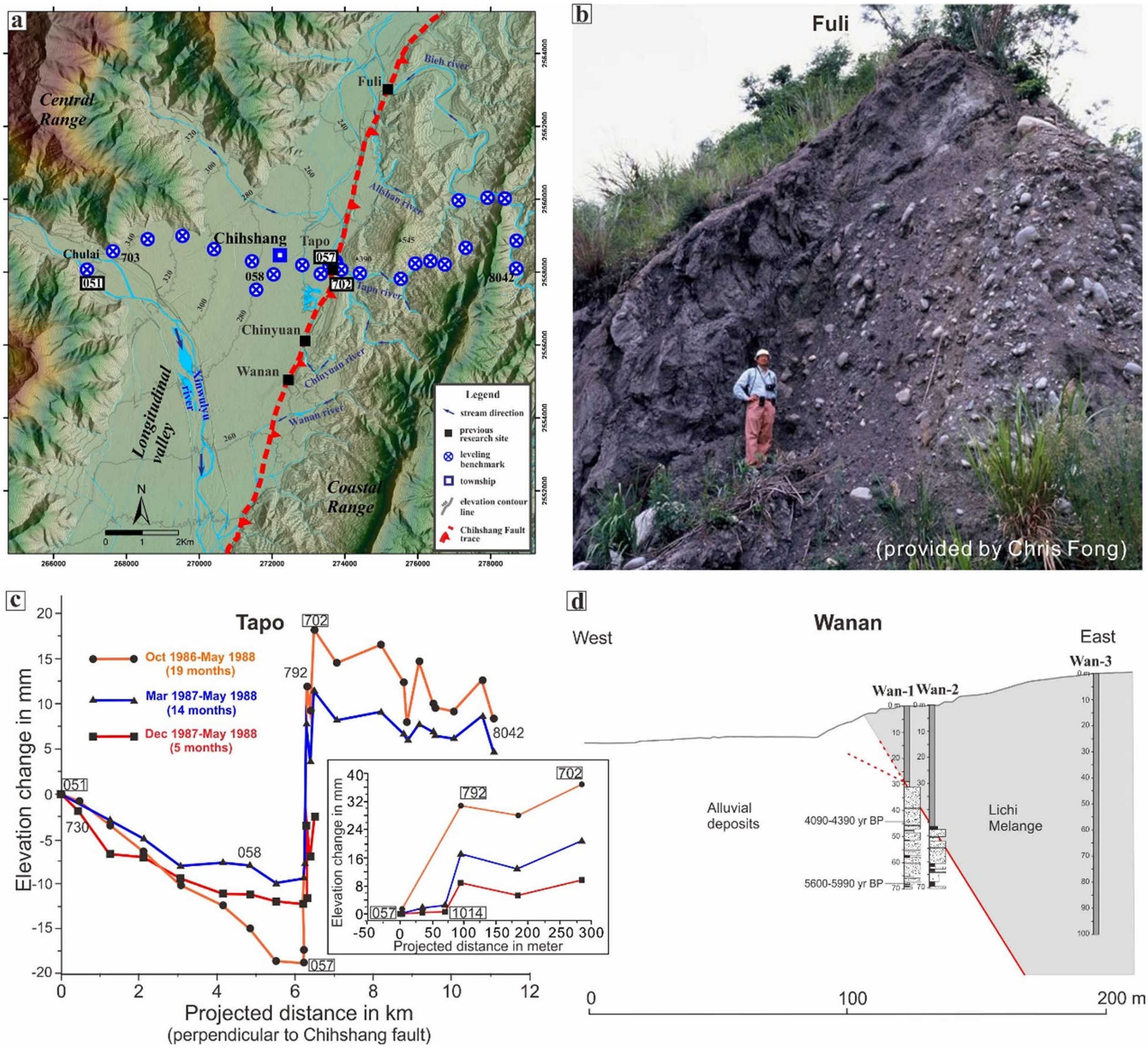

Fig. 2 Characteristics of the ChF. **a** The ChF trace in red located along approximately topographic lineament on 5 m DEM. **b** Outcrop of the ChF at Fuli in 1989. The mudstone of the Lichi mélange is thrusted on top of a gravel layer. **c** Results of leveling measurements in Tapo (modified from Yu and Liu 1989). The locations of the benchmarks are shown in Figure a. Note that an abrupt elevation change appears between benchmarks 792 and 057, at Tapo ES (shown in Fig. 1c). **d** The ChF architecture at Wanan site (after Chen 2008)

the bottom suffered some damage in the form of vertical open cracks (Fig. 3d) and the ground in front of it bulged. These phenomena implied that downward ground movement had also occurred on the slope of the hill.

A decameter-sized debris flow occurred on the slope after heavy rains in April 2016, resulting in a cirque at the edge of the hilltop and a mound of earth along with toppling trees on the stages (Fig. 3e). The mound consisted of mainly aqueous mud across an area of approximately 30 × 20 × 1 m on 16 April, 2016. The cirque exposed a fresh outcrop composed of dominant mud and sparse fragments of sandstone. In addition, there was a sandstone boulder (approximately 1.5 m × 1 m × at least 0.5 m) 10 m east of the cirque in the middle of a paddy field (Fig. 3e), most likely an exotic rock embedded in Lichi mélange before the exhumation to the surface. In late 2018, the remains of the slope failure were wiped away and covered by vegetation (Fig. 3a).

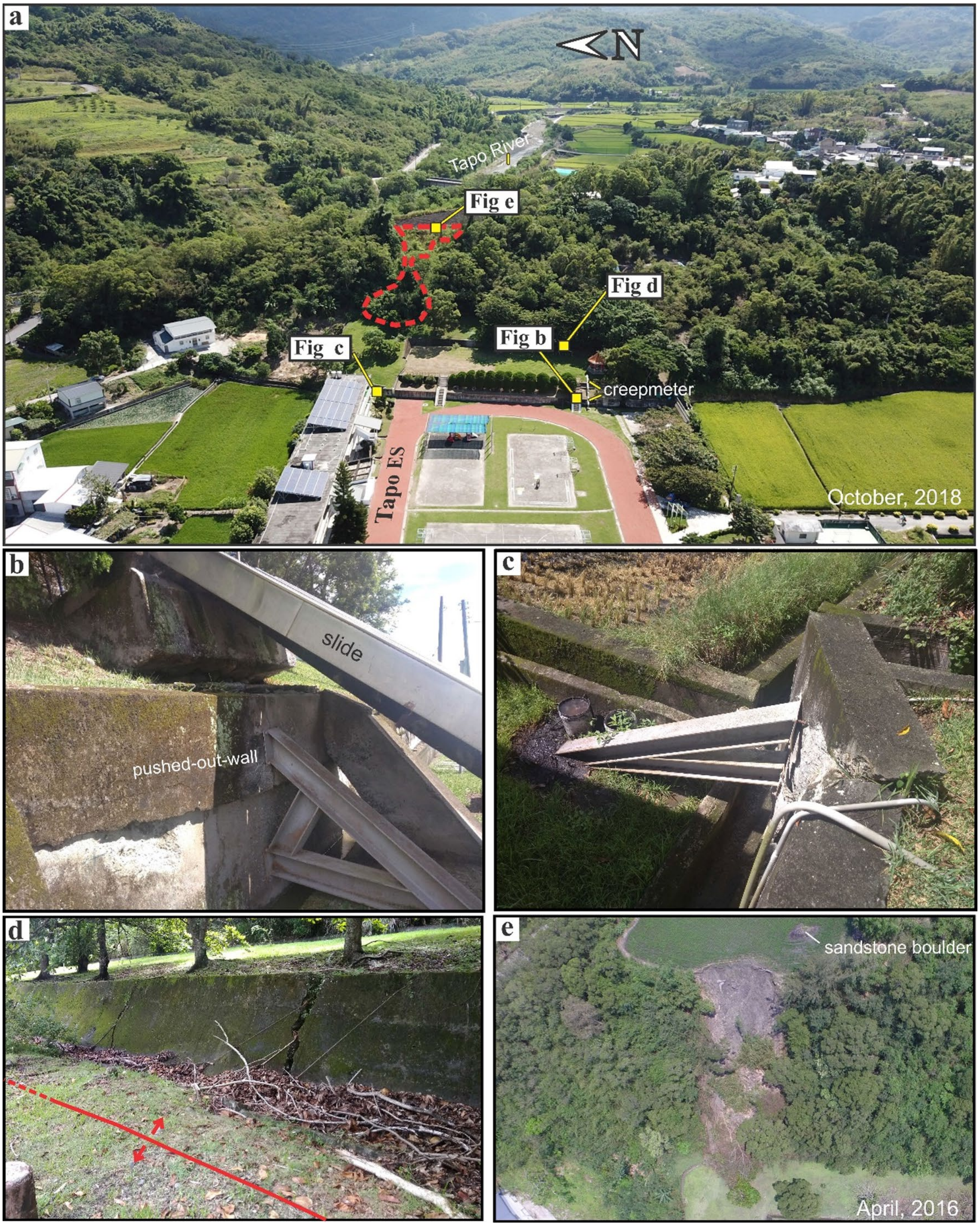

Fig. 3 Surface deformation features on the ChF-line scarp in Tapo ES area. **a** Oblique view of the Tapo ES area. Taken on 5 October 2018 by a camera drone. The red dashed line outlines the remains of the landslide in 2016 (see Figure e). **b** Tilted platform of the slide and bulging wall. **c** Torn apart concrete wall. **d** Cracked concrete wall and bulging ground. **e** A landslide incidence. Drone photo taken on 16 April 2016

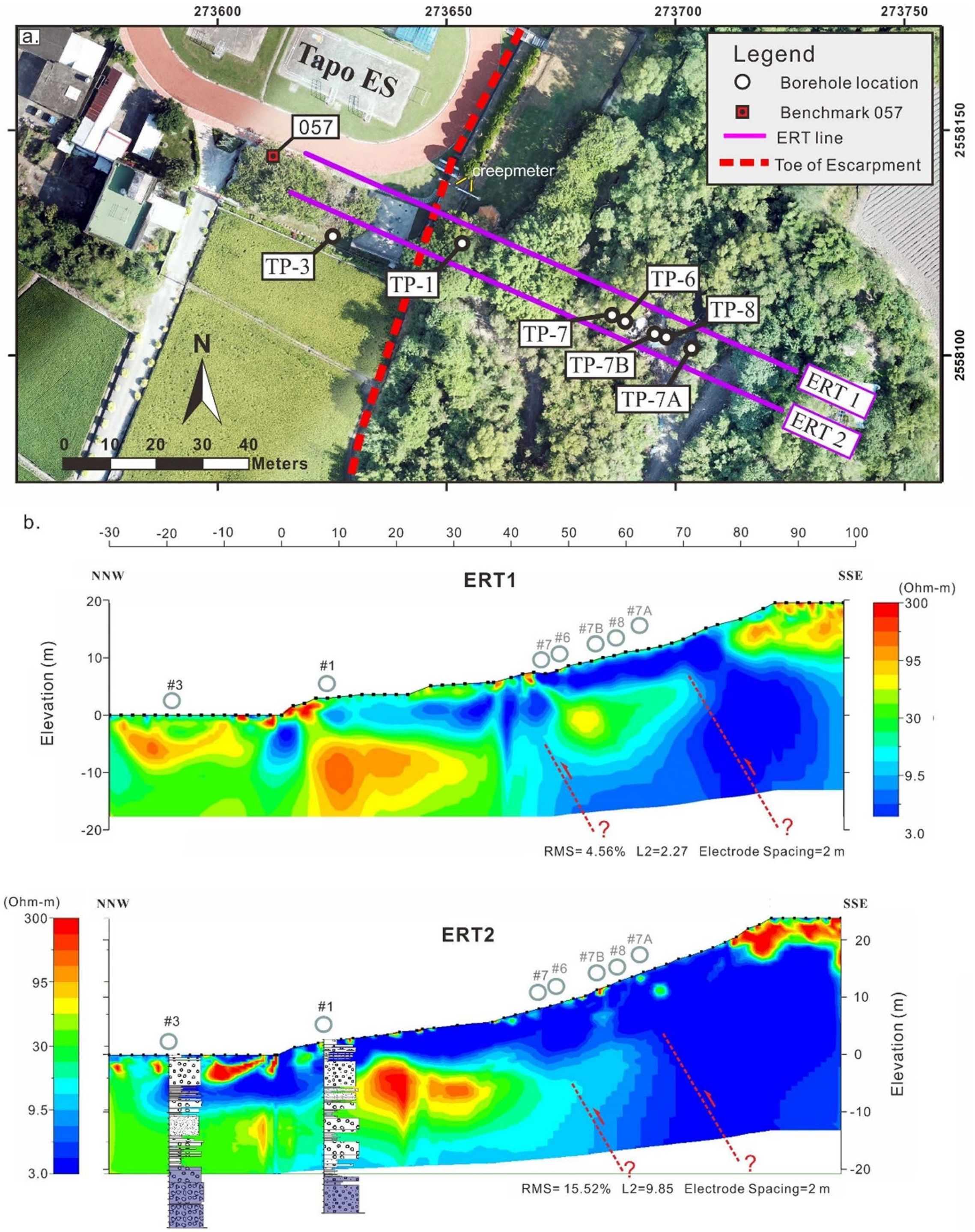

Fig. 4 ERT and boreholes at Tapo ES. **a** Bird's eye view of research area along with configuration of ERT survey lines and boreholes. **b** Inverted resistivity models of ERT 1 (upper) and ERT 2 (lower). Boreholes refer to Fig. 5. The red dashed lines are inferred faults

3 Geophysical and geologic surveys in Tapo ES area

3.1 ERT: Inverted resistivity profile across the geomorphic scarp

The electrical resistivity prospecting method was adopted to obtain a holistic view of the subsurface structure. Two ERT survey lines were deployed perpendicular to the escarpment orientation (Fig. 4) to image the resistivity distribution beneath the surface. These two survey lines, with a distance of 9 m between them are the same as those proposed by Chang et al. (2018). The horizontal span of each line being about 128 m: about 30 m long west of the escarpment and about 100 m long east of the escarpment. The ERT results are presented ahead of other survey data because they provide a regional-scale picture of the fault zone.

3.1.1 ERT deployment

ERT has become a strategic method for detecting blind/concealed active faults at shallow depths (e.g., Nabi et al. 2020; Improta et al. 2010). We carried out ERT using the generalized dipole–dipole array configuration and 64 electrodes in each ERT line. Each array interleaved the positions of the current and the potential electrodes with 2-m electrode spacing. Apparent resistivity data were collected using every possible combination of the four-electrode configurations, then inverted with EarthImager2D™ software (AGI 2009). As suggested by Chang et al. (2018), only ERT data with Wenner and Schlumberger arrays were used for early processing. In this study, a generalized dipole–dipole array was employed, which included Wenner and Schlumberger arrays of Chang et al. (2018). While we acknowledge that the dipole–dipole array may be slightly more affected by cultural noise, the inversion process involving every possible combination of the four-electrode configurations can produce more details of subsurface structures. Consequently, we included data from as many array types as possible, despite the lower computational efficiency. This differed from the approach of Chang et al. (2018), who used fewer array types to streamline the inversion computation which resulted in loss of detail. More detailed terrain information is also used in the inversion process. Due to more types of ERT data, with less sparse sensitivity matrices, the new resistivity models presented in the current study show much finer structures and keep more trends.

3.1.2 ERT results

Based on the inverted model (Fig. 4b), we observed the resistivity value of the research area in the range of 3 Ω-m to 300 Ω-m. In general, models of two ERT survey lines share a common characteristic. The high-resistivity value (> 30 Ω-m) tends to be distributed on the western side, while the low-resistivity value (< 10 Ω-m) tends to distributed on the eastern side of the model. In the middle, the low-resistivity value is on top of the high-resistivity value. One feature that is worth noting is the gradation zone between high-resistivity and low-resistivity area along the profile. The gradation zone appears 40 to 70 m east of the toe of the escarpment. This zone may indicate lithological contact between two different materials or even a fault zone, since the ChF was observed as a contact between the mudstone of the Lichi mélange and the quaternary gravel at other research sites (see Fig. 2b and d). In order to locate the fault and delineate its geometry, boreholes TP-6, TP-7, TP-7A, TP-7B and TP-8 were drilled in sequence. The detailed analyses are presented in the following subsections.

3.2 Core and outcrop lithologic descriptions

3.2.1 Borehole cores and radiocarbon dating data

The rock cores of seven boreholes were documented for this study: TP-1, TP-3, TP-6, and TP-7 are from Chang et al. (2018) and TP-7A, TP-7B, and TP-8 were drilled for the purpose of this research study. We will show later that these new boreholes are crucial because they capture the fault at depth. The boreholes were located as close as possible along the line parallel to the ERT survey lines (Fig. 4a and Table 1) so that the subsurface structure could be deciphered based on the relation between rock core observations and ERT results. We also collected samples of organic sediment and charcoals from the cores that were processed and dated by Beta Analytic Radiocarbon Dating Laboratory in Florida (Table 2). Note that the dating results of the first four samples in Table 2 were adopted from Chang et al. (2018). Radiocarbon dating data are useful for tracing the continuity of layers among the boreholes. Since the ChF has a significant uplift rate, we predicted a significant difference in age in the same level from one borehole to another.

Table 1 Borehole specifications at Tapo ES

Name of the borehole	Coordinate (TWD 97)		Elevation of the borehole upper end (m)	Depth of borehole (m)
	X	Y		
TP-1	273653	2558124	271.2	30
TP-3	273625	2558126	268.5	30
TP-6	273689	2558107	277.4	28
TP-7	273686	2558108	276.7	16
TP-7A	273703	2558102	284.0	82
TP-7B	273696	2558105	280.6	50
TP-8	273698	2558104	280.6	32

Table 2 Radiocarbon dates on the corresponding borehole at Tapo ES

Sample name	Material	Borehole name	Sampling depth (m)	Elevation (m)	Conventional date (yr BP)	Calibrated date (1σ) (Cal yr BP)
CHIHSF-TP1_1270	Organic sediment	TP-1	12.7	261.5	1540 ± 30	1390–1415
CHIHSF-TP3_1585	Organic sediment	TP-3	15.85	252.65	1900 ± 30	1820–1880
CHIHSF-TP6_1475	Organic sediment	TP-6	14.75	265.65	2070 ± 30	1995–2065
CHIHSF-TP6_1955	Organic sediment	TP-6	19.55	260.85	2400 ± 30	2355–2460
CHIHSF-TP7B_2635	Charcoal	TP-7B	26.35	257.25	8910 ± 30	10,006–10062
CHIHSF-TP7B_2947	Charcoal	TP-7B	29.47	254.13	7340 ± 30	8154–8189

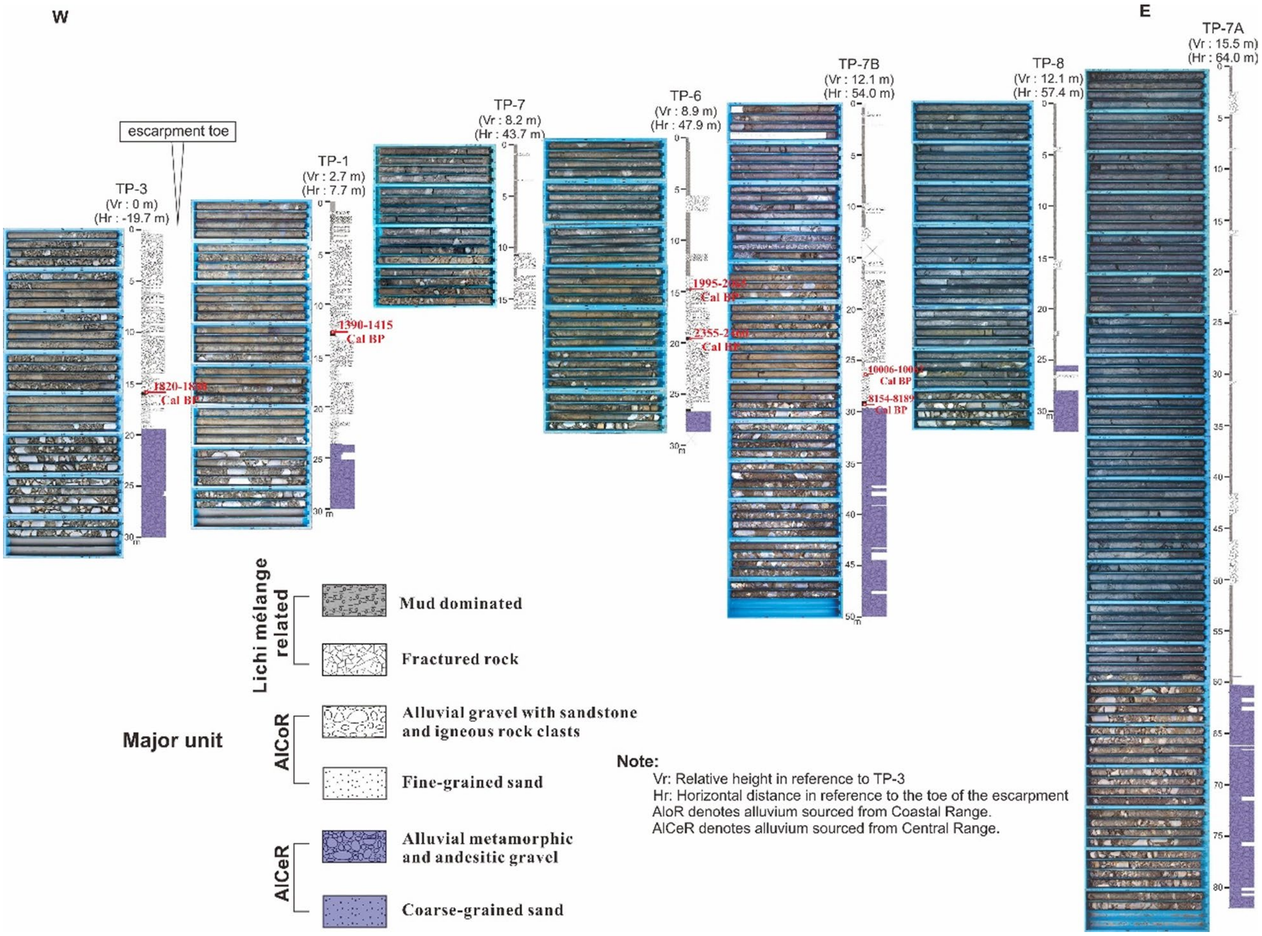

Note:
Vr: Relative height in reference to TP-3
Hr: Horizontal distance in reference to the toe of the escarpment
AloR denotes alluvium sourced from Coastal Range.
AlCeR denotes alluvium sourced from Central Range.

Fig. 5 Rock cores and their stratigraphic columns, arranged according to their spatial locations (Fig. 4a)

3.2.1.1 Lithology of the rock cores The photographs of the rock cores and the stratigraphic columns of all the boreholes are displayed according to their geographic locations in Fig. 5. On the basis of the first-order observation of the rock cores, three lithologic groups are distinguished: (1) Lichi mélange-related rocks/layers, which is mud containing varied types and sizes of rock clasts (Fig. 6a and b); (2) alluvial deposit composed of andesitic gravel layers intercalated with medium to fine-grained sand layers (Fig. 6c); (3) alluvial deposit composed of metasandstone gravel layers intercalated with coarse-grained sand layers (Fig. 6d). Graded bedding and laminations commonly appeared in the last two groups and indicated an alluvial origin. For detailed lithologic descriptions

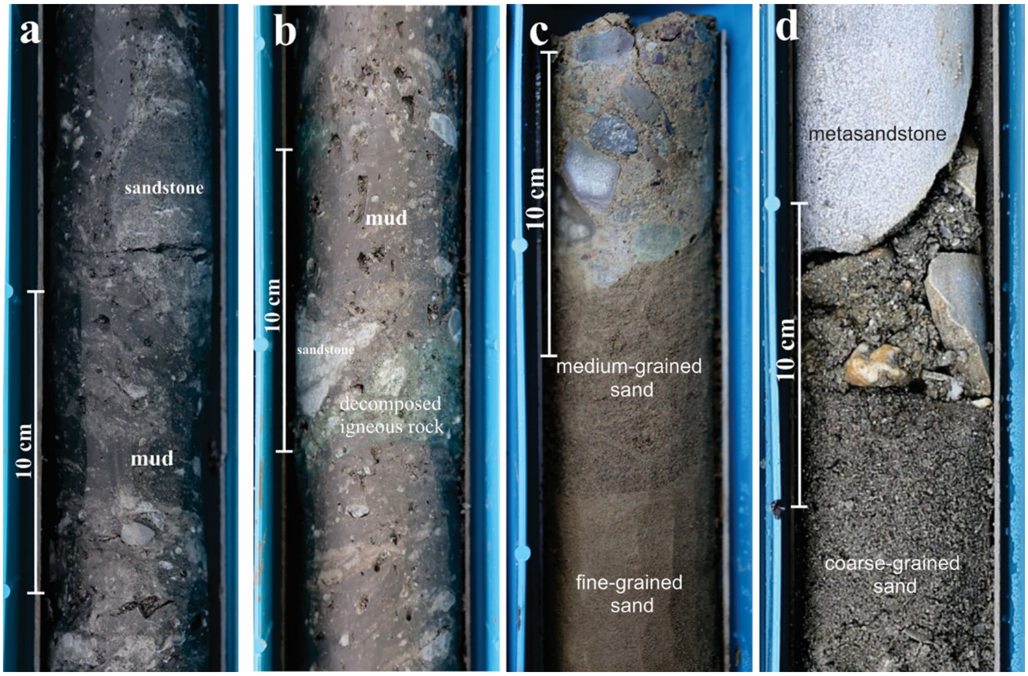

Fig. 6 Texture and lithology of major rock/sediment units from boreholes. **a** Lichi Mélange-related rock at depths of 8.51 to 8.72 m from TP-7. **b** Lichi Mélange-related rock at depths of 5.39 to 5.61 m from TP-6. **c** Coastal Range-sourced alluvial sediment at depths of 12.0–12.23 m from TP-1. **d** Central Range-sourced alluvial sediment at depths of 24.33–24.57 m from TP-1

of these rock cores, refer to Fitrianto (2020). We inferred that the alluvial deposit containing andesitic gravel and fine-grained sand was sourced from the Coastal Range, where volcanic and sandstone formations are dominant, and was likely transported by the Tapo River (Fig. 2). We labeled such alluvial deposit as AlCoR (Alluvium sourced from Coastal Range) for later use. Meanwhile, we inferred that the alluvial deposit dominated by metamorphic clasts was sourced from the Central Range composed of metamorphic rocks and was likely transported by the Xinwulyu River because it is a nearest river and transects the Central Range (Fig. 2). Thus, we labeled such alluvial deposit as AlCeR (Alluvium sourced from Central Range). Roughly speaking, the sequence of these three groups is AlCeR, AlCoR and Lichi mélange-related layers from bottom to top in all boreholes (Fig. 5). However, AlCoR was noticeably absent from boreholes TP-8 and TP-7A. Furthermore, TP-7B, TP-8, and TP-7B from west to east were drilled 50, 32 and 82 m in length, respectively, to explore the ERT gradation zone 40 to 70 m east of the toe of the escarpment (Fig. 4). From the core observation of these three boreholes, high-angle lithologic contacts, which are most likely faults, were found at depths of 15.4 m in TP-7B, 27.9 m in TP-8, and 60.3 in TP-7A (Fig. 7). Based on their locations, the fault angle is estimated as 75° ~ 78° via trigonometry.

3.2.1.2 Characteristics of in situ Lichi Mélange and Lichi Mélange-derived rocks/layers We found two general characteristics of the Lichi mélange-related mudstone: irregular texture and sheared texture. These textures are differentiated by the presence of lenticular assemblages. For the sheared texture, we found that these lens-shaped materials dominated and were distributed within the mudstone in a preferred orientation (Fig. 8b and d). According to field observations around the Bieh River by Chang et al. (2001), the in situ Lichi mélange is strongly sheared mud with striated foliation. Thus, we inferred that the mudstone with sheared texture is the in situ mélange. Meanwhile, mudstone with irregular texture did not have any shear pattern (Fig. 8c) and is denoted as reworked mélange in this study. Most such mudstones were found near the surface at depths above 10 m in five cores: TP-6, TP-7, TP-7A, TP-7B, and TP-8 (Fig. 8a). We suspected that they were of the in situ Lichi Mélange reworked by near-surface process, such as landslides, debris flows in particular, which transformed their sheared texture into irregular texture.

We also found the presence of breccia and gouge within the mélange (Fig. 8b). Most of these brittle fault rocks (Sibson 1977) are present along the inferred Chihshang main fault. These fault rocks likely resulted from main fault activity. In TP-6, the fault rocks appeared

Fig. 7 Fault contacts/fault zones in the rock cores. Red lines highlight the mixed zone/fault zone between Lichi Mélange and alluvium deposit. Yellow polygons denote deformed alluvium deposits in the Lichi Mélange. **a** Rock core of TP-7B at depths of 12 to 20 m. **b** Rock core of TP-8 at depths of 21 to 29 m. **c** Rock core of TP-7A at depths of 56 to 64 m. **d** Fault contact between mud of Lichi mélange (at right) and fine-grained sand of alluvium (at left) in TP-7B at depth of 15.4 m. **e** Fault contact between mud of Lichi Mélange (at right) and fine-grained sand of alluvium (at left) in TP-8 at depth of 27.9 m. **f** Fault contact between mud of Lichi Mélange (at left) and very coarse-grained sand of alluvium (at right) in TP-7A at depth of 60.3 m

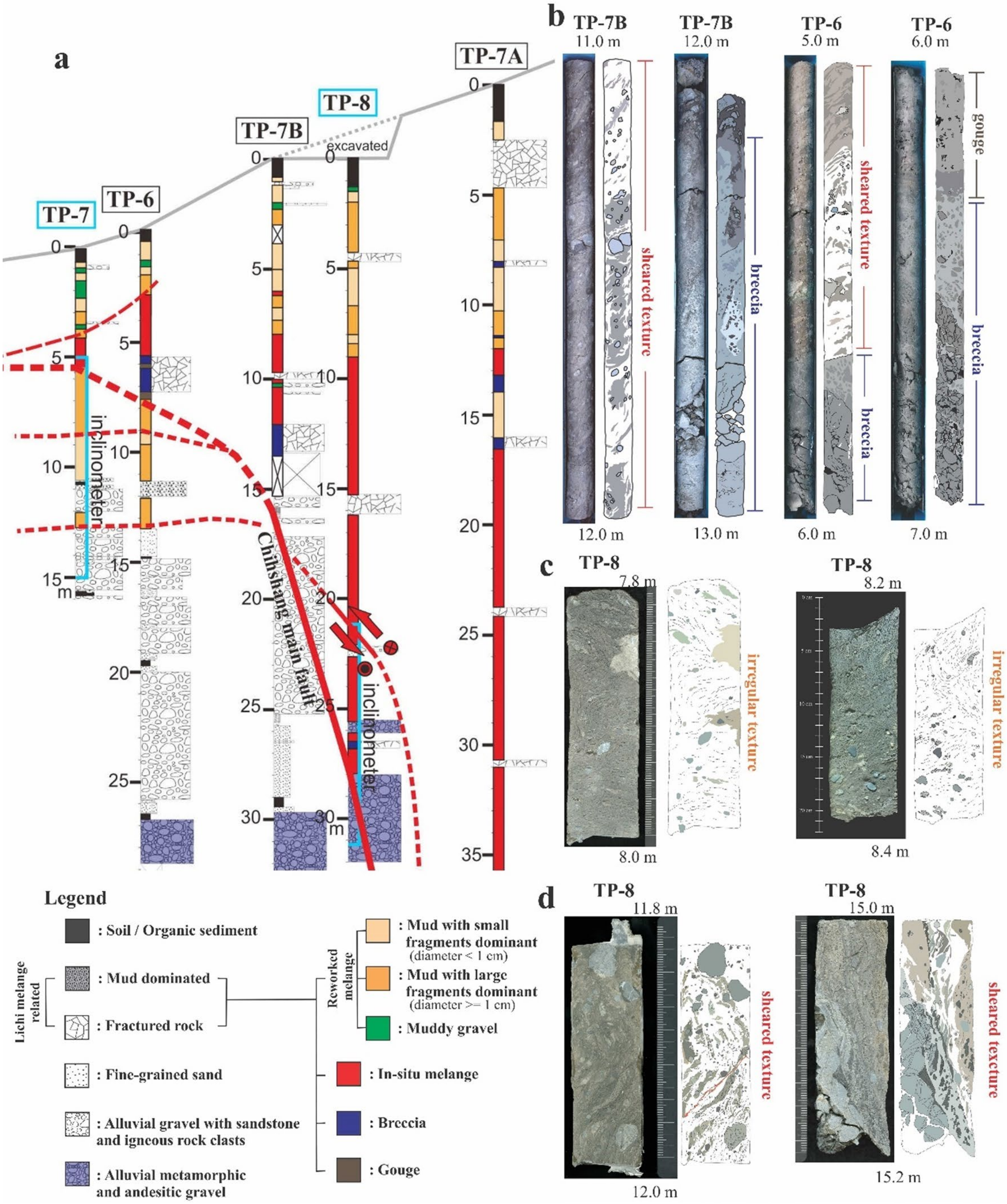

Fig. 8 **a** Core logs along with textural classification of Lichi Mélange-related rocks. Red lines are fault traces. The thin continuous-dashed red line with offset ornamentation is based on inclination data, and the thick solid/dashed line is based on core observations. The uppermost thin dashed red line is a sole slipping surface inferred from core observations. Refer to Session 3.2.1.2 for more explanations of how to recognize the traces. The blue lines attached to TP-7 and TP-8 indicate the depths where an inclinometer was installed. **b** Rock cores and their sketches. **c** Irregular texture on bisected core surfaces. **d** Sheared texture on bisected core surfaces. A red line denotes a shear plane

on top of reworked mélange at a depth of 7.5 m (Fig. 8a). Thus, we inferred that the Chihshang main fault not only juxtaposed the Lichi Mélange and alluvium, but also cut into the reworked mélange with decreasing dip angle as it approached the free surface (Fig. 8a).

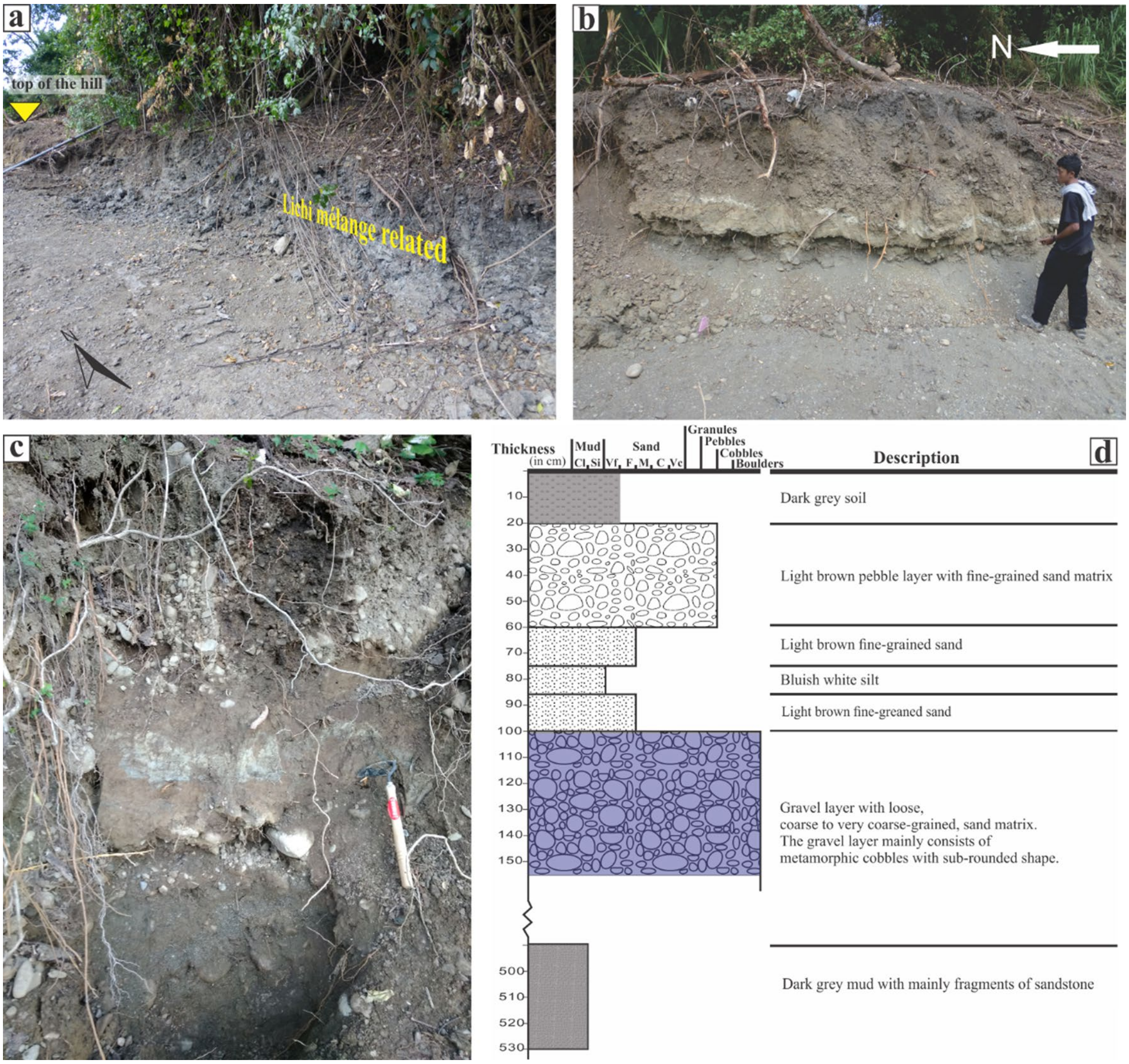

Fig. 9 Outcrops near the hill top east of Tapo ES. **a** Mudstone of Lichi Mélange. **b** Horizontal layered sediment vertically exposed at the western edge of the hill top. **c** Close-up of the layered sediment. **d** Stratigraphic column of the outcrops

3.2.2 Alluvial deposits at the top of the hill

The hill abutting the Tapo ES is densely covered by vegetation except for the recreation area (Figure 3a). The hillslope south of the recreation area has a moderately steep angle ranging between 10° and 30° and increasing uphill. Under such conditions, an excavation to create an access road was necessary so that a drilling machine could be transported to certain positions on the slope. This excavation created not only an access to the drilling sites, but also new exposure and an access to outcrops hidden in the hill. The new exposure consisted of mélange-related material containing mainly mud with fragments of sandstone (Figure 9a). An outcrop of sedimentary deposit (Figure 9b) was found on the slope close to the hilltop. The upper deposit was thickly bedded alluvial layers sourced from the Coastal Range; one andesitic gravel layer and two fine-grained sand layers intercalated with one medium bedded silt layer (Figure 9c). This was capped by dark soil. The total thickness was approximately 1 m. Further down, there appeared alluvial layer sourced from the Central Range. This alluvial layer contained metamorphic cobbles with a very coarse-grained sand matrix. The thickness of this alluvial layer was at least 0.5 m without reaching the lower boundary. However, if we considered the mélange-related material exposed on the road cut next to this outcrop (Figure 9a), we could approximate the appearance of mélange-related material at a depth of 3 m below the alluvial layer. This estimation was also supported by ERT, which showed a high-resistivity stripe on the hilltop (Figure 4b). The above-mentioned observations corroborated

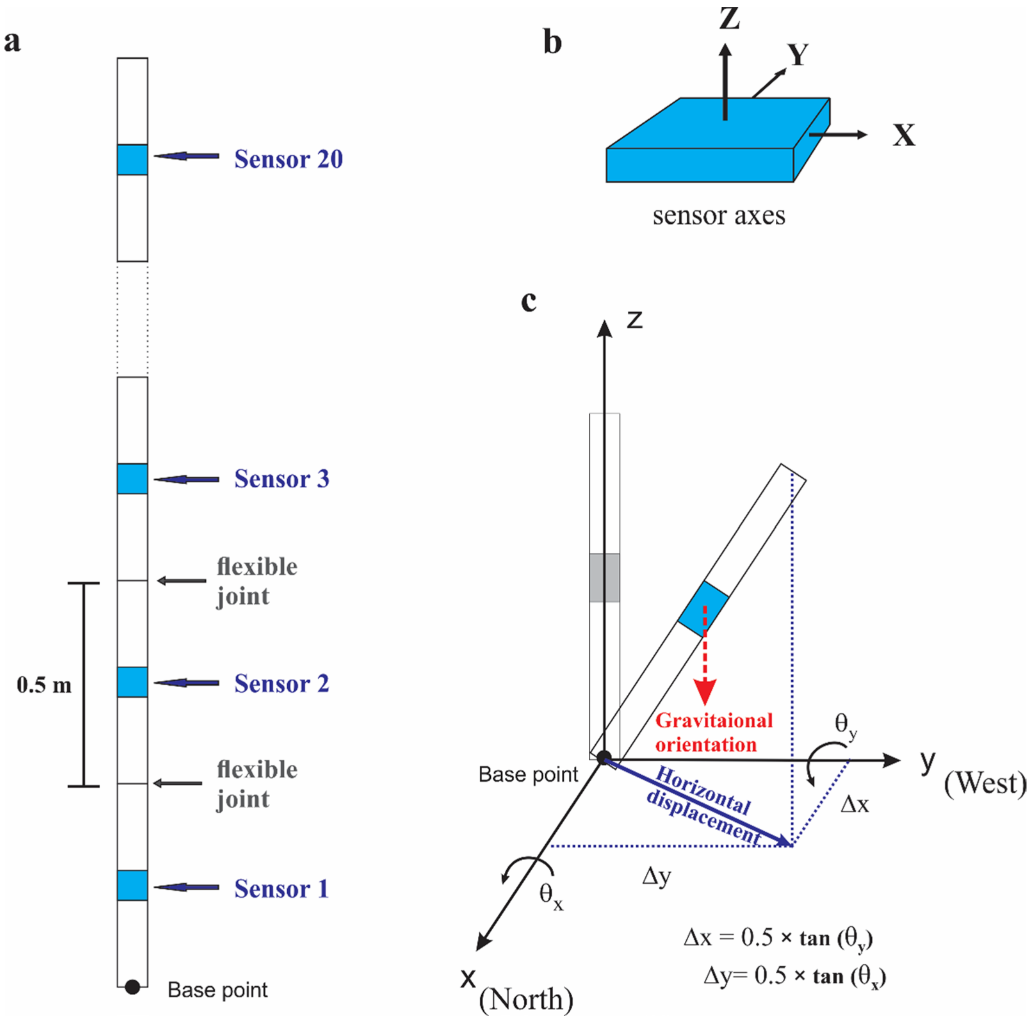

Fig. 10 Measurement principles of SAAF inclinometer (after Abdoun et al. 2007 and Measuring Inc., 2021). **a** Schematic of SAAF arrangement. **b** Sensor axes. **c** Principle of displacement measurement by SAAF

the authenticity of a cross section constructed in the next section.

3.3 Borehole inclinometer

3.3.1 Data acquisition and processing

We installed one unit of Shape Accel Array Field (SAAF) into the boreholes to monitor the subsurface deformation. SAAF is a string of rigid segments separated by flexible joints. The total length of SAAF was 10 m with segments of 0.5 m each. In each segment, there was a Micro Electro Mechanical Systems (MEMS) sensor, which measured the tilt angle relative to gravity's direction and then converted the tilt angle into horizontal displacement via trigonometry (Fig. 10).

Monitoring data were collected from boreholes TP-7 and TP-8 (Fig. 8) where the inclinometer was installed at depths of 5 to 15 m for TP-7 and at depths of 21.3 to 31.3 m for TP-8 over two different periods. In TP-7, the monitoring period was from 6 May 2016 to 10 October 2018, with a sampling rate of 5 min, while in TP-8 the monitoring period was from 19 October 2018 to 27 May 2021 with a sampling rate of 10 min. Long-term accuracy is ± 1.5 mm based on the field measurements of vertical SAAF over 1.5 years of operation, as stated in the SAAF manual of the Measurand Company. The oscillation of the data from individual sensors in our own inclinometer was within 0.5 mm (examples shown in Fig. 11a and b). Each of the two datasets was used only for a 2-year duration to avoid instability in the early installation and before decommissioning of the inclinometer. The 2-year durations were from 1 July 2016 to 30 June 2018 for TP-7 and from 1 January 2019 to 31 December 2020 for TP-8.

Considering the abundance of data, we derived mean values from daily data for all individual segments. Then, we smoothed the daily means to eliminate any outliers and find a regression curve to fit them, shown

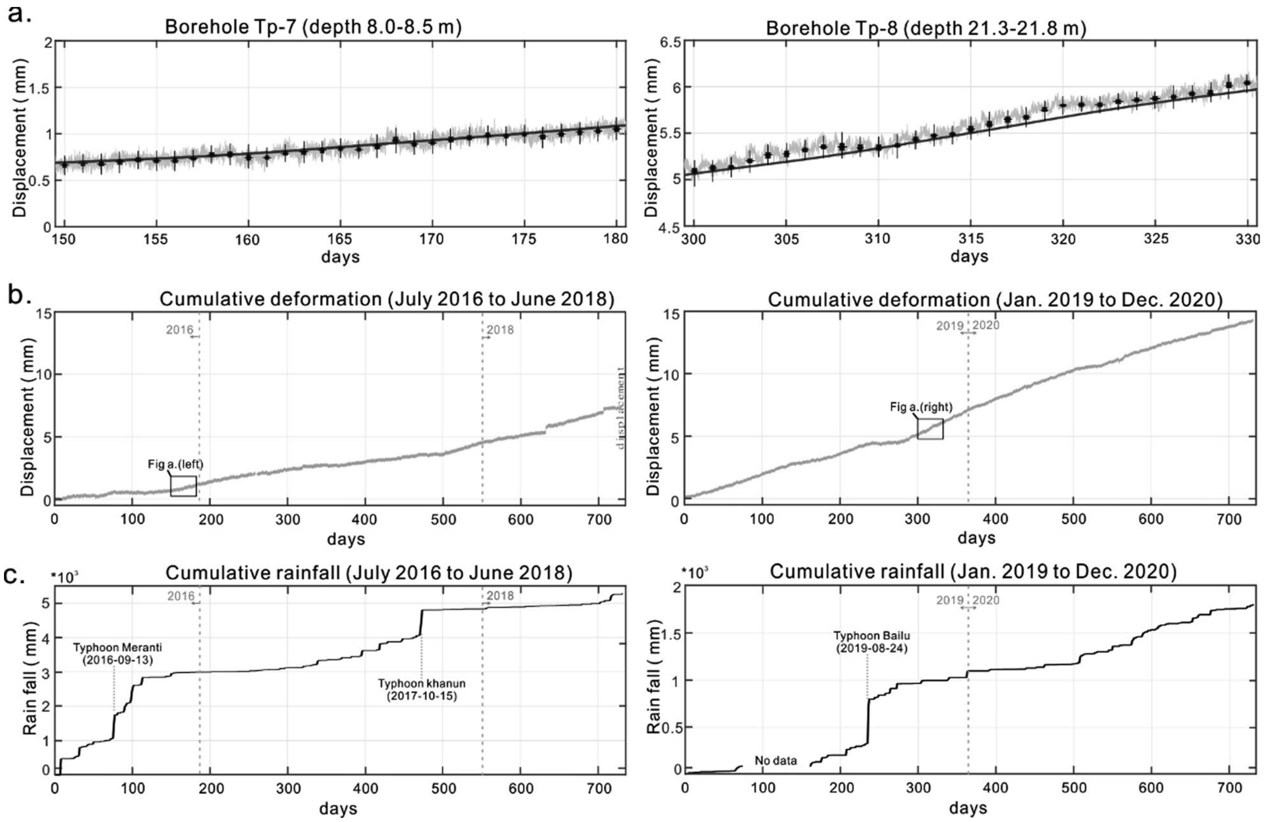

Fig. 11 Subsurface deformation and rainfall in Tapo. **a** Oscillation and trend of the data from two individual inclinometer sensors. **b** Two-year cumulative deformation for the same two individual segments derived from inclinometer monitoring. **c** Two-year cumulative rainfall. Data source was the Chihshang rainfall station of Taiwan Central Weather Bureau, the location of which is shown in Fig. 1b

as black curves in Fig. 11a. Based on the derived regression curves, we attained the relative displacement of a specified segment over a specified time period in reference to the base point of the inclinometer (Fig. 10c).

3.3.2 Subsurface deformation

Figure 12 shows the plots of cumulative displacement with depth for all segments of the inclinometer installed in TP-7 and TP-8. Displacement increments are shown with intervals of 3 months over the 2 years. The inclinometer was set to depths of 5 to 15 m of TP-7 to confirm whether the contacts of the Lichi Mélange-related material and AlCoR (Fig. 8a) were actively moving. The cumulative horizontal deformation at depths of 5 to 15 m of TP-7 was 34.7 mm towards the north and 6.2 mm towards the west over the two years (Fig. 12a). The relatively intense northward movement occurred at depths of 13.5–13.0, 12.5–12.0, and 9.0–8.0 m and stable northward movement occurred at depths of 7.5 to 5.5 m. Interestingly, the bottommost contact of the two lithologic groups was located at a depth of 12.7 m within the segment in between the two active segments. The rock core at depths of 13.5–13.0 m was composed of sandy gravel with no obvious shear plane or zone. The rock core at depths of 12.5–12.0 m was mainly composed of reworked mélange and a subhorizontal gouge zone of ~ 2 cm thickness was observed at a depth of 12.3 m (Fig. 13b). In contrast, although the rock core at depth of 9.0–5.5 m was also composed of reworked mélange, no obvious shear plane or zone could be identified. Likely, the intense deformation was distributed over a wide range.

The inclinometer was utilized at depths of 21.3 to 31.3 m of TP-8 to confirm whether the main fault was actively moving. Distinct displacement gradients were observed at depths of 25.8 to 22.3 m for the North–South component and at depths of 27.3 to 23.3 m for the West–East component. Roughly, the depth range corresponded to the main fault-affected zone at depths of 28.0–22.1 m (Fig. 7). Such small amplitudes of horizontal deformation and changing displacement gradients may have resulted from the highly steep fault with a dip of greater than 75° (Fig. 8) and the complexity of its affected zone (Fig. 13d), which was two sections of alluvial materials from the footwall embedded in the sheared mélange within the zone (Fig. 7b) and two high-angle faults side by side at depths of 22.2 to 22.5 m (Fig. 13d) in the upper section.

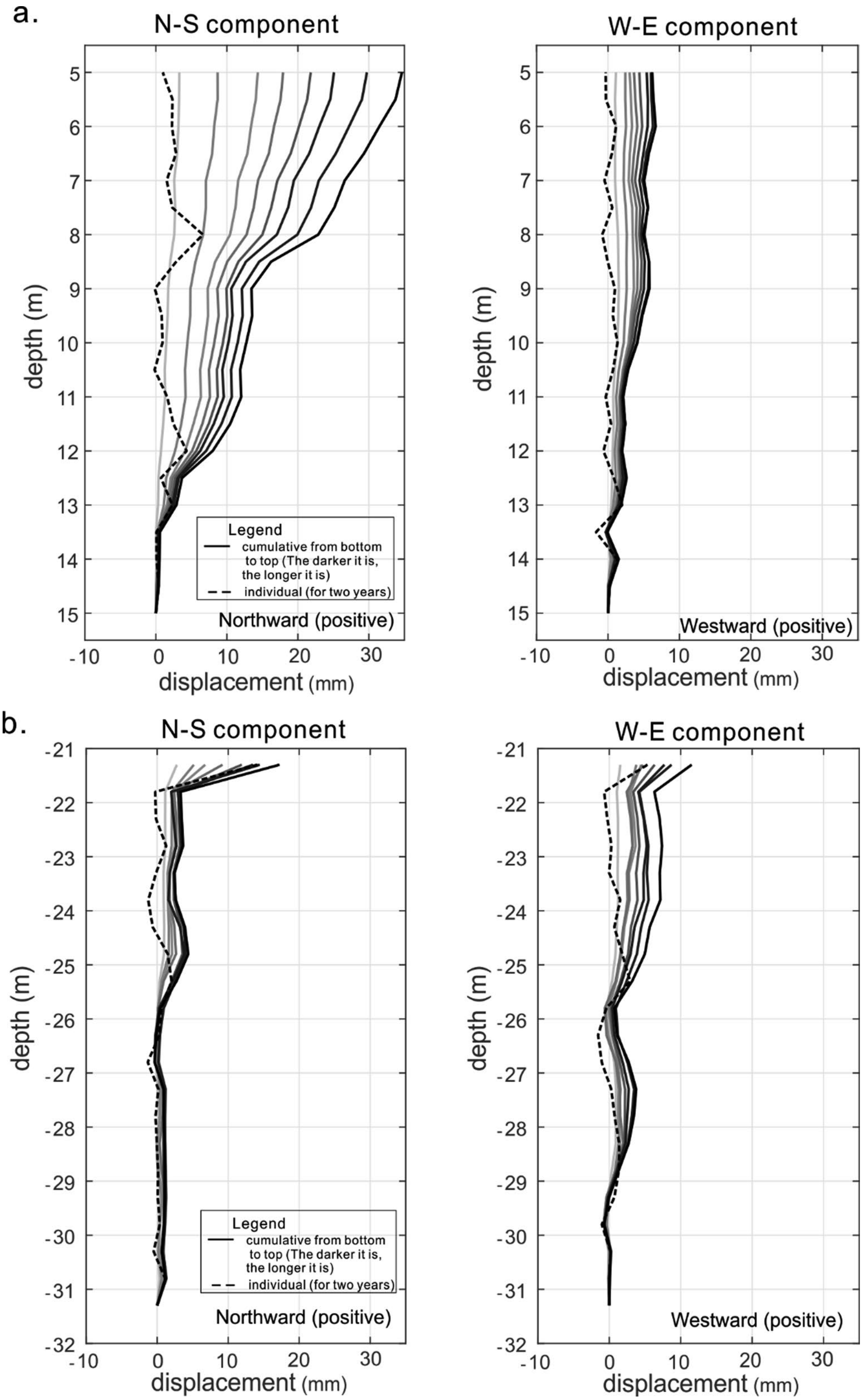

Fig. 12 Subsurface deformation recorded via inclinometer. Cumulative displacements with depth are shown with intervals of 3 months over the 2 years in addition to cumulative displacement of individual segments over 2 years. Individual segments were all 0.5 m long. **a** Relative displacement at depths of 5 to 15 m in TP-7 from 1 July 2016 to 30 June 2018. **b** Relative displacement at depths of 21.3 to 31.3 m in TP-8 from 1 January 2019 to 31 December 2020

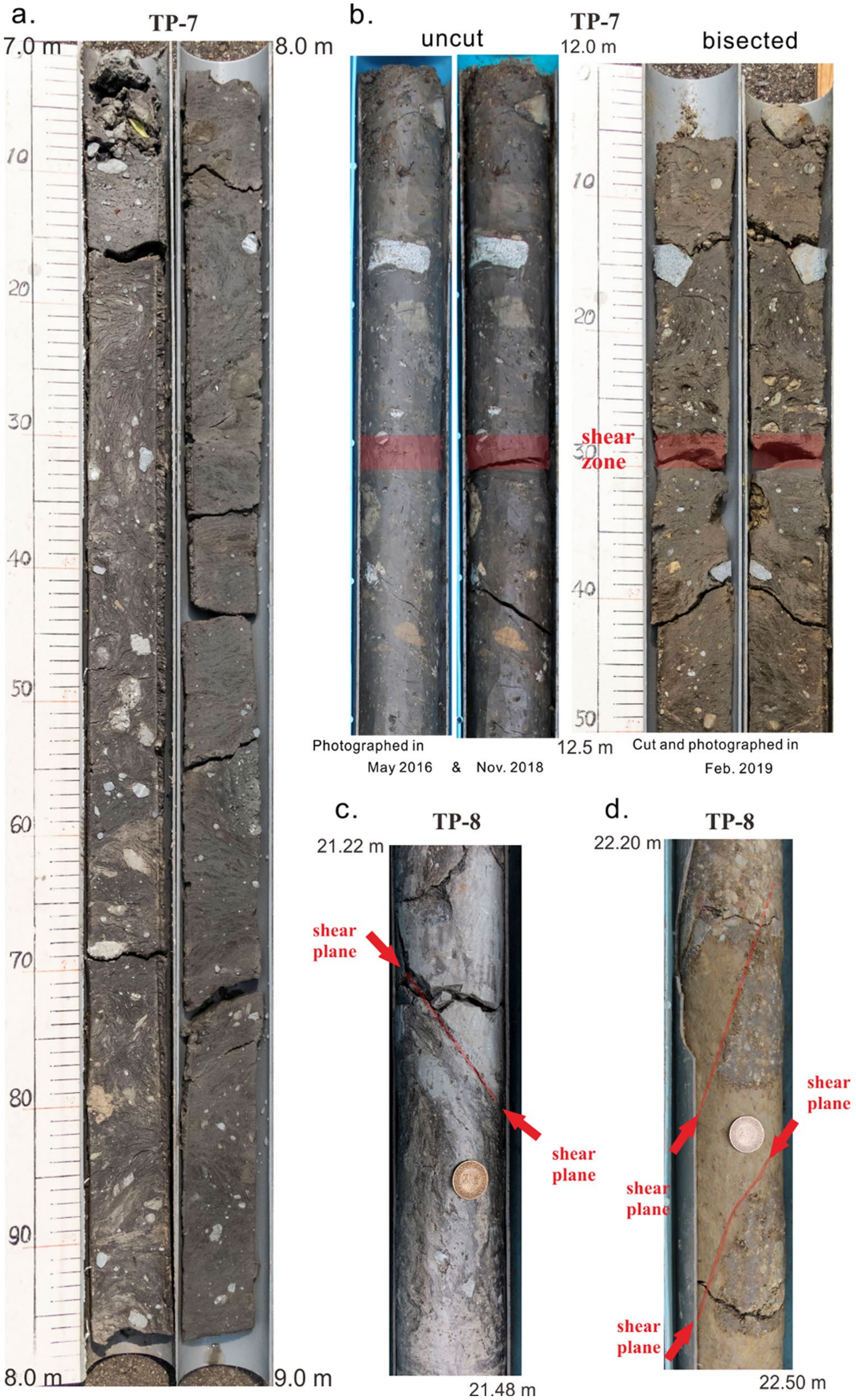

Fig. 13 **a** Bisected surface of reworked mélange core of TP-7. It is mainly composed of mud with large fragments for the bisected core at left and small fragments at right. **b** Tabular shear zone at depths of 12.3 m of TP-7. **c** Shear plane within the mélange at depth of 21.3 m of TP-8. **d** Shear planes at depths of 22.5 to 22.2 m of TP-8

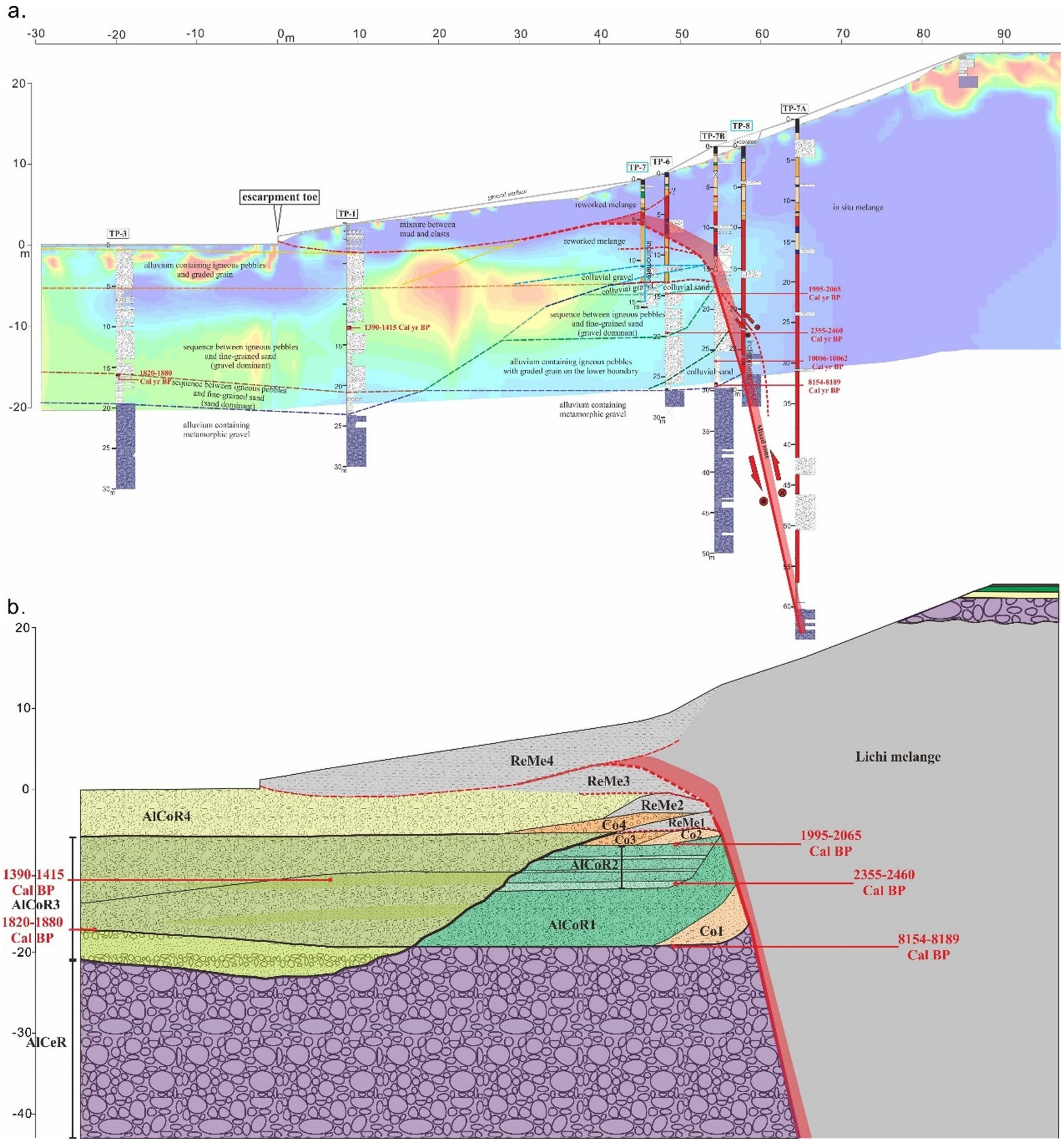

Fig. 14 Cross section perpendicular to the ChF at Tapo ES. **a** Integrated cross section along the ERT-2 survey line. The location of ERT-2 survey line is shown in Fig. 4. **b** Illustration of geologic section. The red bold line indicates the Chihshang main fault. Red labels indicate the dating data at the corresponding spots where the samples were collected. The abbreviations are denoted as follows: AlCeR is alluvium sourced from Central Range; AlCoR is alluvium sourced from Coastal Range; ReMe is reworked mélange; Co is colluvial deposit

Relatively intense northward and westward movements occurred at depths of 21.8–21.3 m, with amplitudes of 13.9 mm and 5.2 mm, respectively. Accordingly, a distinct shear plane with a dip angle of 56° was observed at a depth of 21.23 m (Fig. 13c). The cumulative horizontal deformation composed of 17.2 mm towards to the north and 11.5 mm towards the west was accommodated by faulting on this shear plane, with 80.8% northward movement and 45.2% westward movement, respectively (Fig. 12b).

4 Synthesis: Structure and stratigraphy integration

We constructed the subsurface structure by stratigraphic correlation among the boreholes (Fig. 14). This correlation was based on the principle of sedimentary original horizontality and the consideration of dating data along with the ERT images. The escarpment had been largely inferred as a fault scarp of the ChF at Tapo ES as mentioned previously. We did not find diagnosable difference in these two boreholes, i.e., TP-1 and TP-3. Both of them showed that the AlCoR unit was above the AlCeR unit (Fig. 5). The lithological contact of these two units was observed in both TP-1 and TP-3 with a depth level difference of about 1.5 m while the horizontal distance was about 28 m. Furthermore, based on the dating data of AlCoR unit from these two boreholes, we found the shallower layer to consistently be of a younger age, 1390–1415 Cal BP, than the deeper layer, 1820–1880 Cal BP. This result did not provide any evidence about the presence of an active fault directly beneath the escarpment.

The gradation zone ranged from 40 to 70 m in the ERT profiles (Fig. 4b and Fig. 14a) as mentioned previously and became our target for fault contacts. The five boreholes TP-7, TP-6, TP-7B, TP-8 and TP-7A from west to east were vertically drilled 16, 28, 50, 32, and 82 m in length within the gradation zone, respectively. TP-7 and TP-6 were about 3 m from each other. The rock cores of these two boreholes were correlative. They both showed that the Lichi mélange-related layers lie on the AlCoR and a small unit of the AlCoR is intercalated in the Lichi mélange-related layers less than 2 m above the bottommost contact of these two lithological groups. The bottommost contacts of these two lithological groups were almost on the same level in these two boreholes. There is no phenomenon related to our expected result for the inclined shear plane or zone of the ChF. TP-7B and TP-7A were 10 m from each other and TP-8 was in between them, 3.4 m east of TP-7B. Based on these three boreholes, we inferred earlier that the Chihshang main fault is a lithological contact of alluvium deposit and Lichi mélange with a dip angle of 75° to 78°. We also observed the presence of alluvium material intercalated with the Lichi Mélange near these lithologic contacts in all three boreholes. The vertical lengths of these fault-affected zones are at least 0.8 m in TP-7B, 6.9 m in TP-8 and 1.2 m in TP-7A (underlined in red in Fig. 7). This feature likely formed as the result of the fault activity that deformed the footwall materials, in this case alluvial deposits, and then became mixed in with the hanging-wall mélange material.

In general, the underlying alluvium containing metamorphic gravel (AlCeR) is relatively easy to correlate, because it has distinguishable characteristics, including occurrences of metamorphic cobbles and sediment of very coarse-grained sand, etc. By tracing the AlCeR upper boundary, we found a depth level difference of approximately 3 m, from TP-1 to TP-6. From the dating data of the AlCoR, we also found evidence of non-horizontality. In TP-1 and TP-3, the date range is 1390 to 1880 Cal year BP, while in TP-6, at relatively shallower depth, the date range is 1995 to 2460 Cal year BP. The difference in the depth level from TP-3 to TP-6 is approximately 15 m. However, this result does not correspond to the depth level difference of AlCeR upper boundary. One reason for this observation may be the erosion occurrence that wiped away some portions of AlCoR2 and AlCoR1 and the upper part of AlCeR (Figure 14b). Some part of the older alluvium was eroded, then the younger alluvium was deposited on top of the remaining older alluvium.

In between TP-7B and TP-8, we also observed a depth level difference in the upper boundary of AlCeR. In this case, the presence of a branch fault is possible since this part is close to the Chihshang main fault. However, there was no evidence of the fault plane of the branch fault from the core (Figs. 8b and 14). Thus, we inferred that in this part, the layers had been folded into a drag fold due to the activity of the main fault. This was supported by alternating layers of sand and mud at depths of 29.5–28.5 m of TP-7B that were titled at an angle of 37°. This sequence of very thinly alternating beds of mud and sand on the AlCeR layer was likely overbank sediments. On top of it, we observed thick clayey fine-grained sand layer at depths of 29.5–25.1 m. The inter structure of this layer was chaotic instead of stratified. One layer with the same characteristics was also observed in TP-6 at depths of 26.4–25.9 m, similarly, on top of inferred overbank sediments. However, in TP-6, this layer was much thinner compared to that observed in TP-7B. We inferred that this type of layer is the product of slope processes known as colluvial deposit. This feature was also observed at shallower depth, in TP-6 at depths of 14.7–13.5 m and TP-7 at depths of 14.3–14.0 m.

In TP-6, at depths of 25.5-20.0 m (Figures 8 and 14), we observed a thick gravel layer, AlCoR1, containing andesitic and sandstone pebbles, above the colluvial deposit mentioned above. This layer laterally continued to TP-7B at depths of 25.1-17.1 m. In TP-8, approximately 3 m east of TP-7B, this gravel layer was totally replaced by in situ mélange at the corresponding depth.

We inferred that part of the gravel layer had been cut and uplifted due to ChF activity and then eroded away.

Above the aforementioned gravel layer, AlCoR1, the overlying material in TP-6 at depths of 20.0-14.7 m (Figure 8) is the sequence of andesitic gravel layers with intercalated fine-grained sand layers, AlCoR2 (Figure 14). Based on carbon-14 dating, this sequence started to settle 2355 to 2460 cal yr B.P. (Figure 14). If we correlate TP-6 and TP-7, this layer can be traced horizontally, which indicates no active fault in between these two boreholes. In TP-7B, this sequence is mainly replaced by the mélange-related materials above the gravel layer, AlCoR1 (Figure 14). Above this sequence in TP-6, we observed two different colluvium settlements: colluvial sand and colluvial gravel. Based on the dating data, these colluvial sediments settled at most 1995 to 2065 cal yr B.P.

In TP-6 and TP-7, we observed the sequence of reworked mélange with interbedded colluvial gravel at depths of approximately 10 to 14 m. Based on the displacement recorded by the inclinometer at this depth level in TP-7, we inferred minor active branches of the ChF, which contributed to the deformation within the reworked mélange. Furthermore, the in situ mélange at shallow depths in TP-6 and TP-7 was overlain by the reworked mélange. From the tracing of the boundary between the in situ and reworked mélange, we inferred that a slipping sole plane of the reworked mélange truncates the in situ mélange and overprint the upper tip of the Chihshang main fault.

In TP-1, we observed a mixture of mud with rock clasts at depths of 3.8-0 m. This mixture was similar to the reworked mélange, but clasts are more dominant. A piece of concrete was observed at a depth of 0.8 m along with small pieces of brick fragments elsewhere within the mixture. We suspect that this mixture was formed as the result of stirring reworked mélange and alluvium deposits due to the construction of the pavilion or/and drainage close to the site of TP-1 (Figure 4). A strong argument for this cause was an excavated exposure along the escarpment at Tapo ES in May 1997 before the installation of a new retaining wall, which was reported by Chu et al. (1998). The excavated surface showed dark grey Lichi mélange-related material on top of yellowish-brown alluvium with a fault contact approximately 0.5 m high in reference to the flat ground in front of the escarpment. The fault strikes parallel to the escarpment and dips approximately 10° to east. This exposure, combined with the ERTs, contrives to delineate a basal slip surface beneath the reworked mélange at shallow depth. Based on the above-mentioned correlations, we illustrate the section model of the Chihshang main fault in the Tapo ES area (Figure 14b).

5 Discussion

5.1 Structure and deformation at the ChF-line scarp

5.1.1 Dip angle of the main fault along the strike and its surface trace location relative to the toe of the escarpment

Previous geologic studies (e.g., Hsu 1962; Angelier et al. 2000; Lee et al. 2003; Lin et al. 2009; Mu et al. 2011) and geodetic surveys (e.g., Yu and Liu 1989; Yu and Kuo 2001) have shown that the ChF is an active left-lateral reverse-slip fault. Given that the sense of faulting is known, the two other important parameters are fault angle and location of its surface trace or upper tip in view of damage mitigation within faulting-induced deformation zones. Paleoearthquake studies (McCalpin and Caver, 2009) have shown that active faults commonly displace the ground repeatedly at the same surface locations or nearby. Such a phenomenon is extremely important for precisely locating the fault surface traces. Another important aspect is the effect of the dip angles of active faults, in particular, at the shallow depth of hundreds of meters, which affect the patterns of deformation and width ratio of deformation zone in hanging wall to the one in the footwall while transient fault slip occurs (Huang 2006; Huang and Johnson 2010; Chang et al. 2015). For example, based on an elastic–plastic model of fault slip propagation for formation of deformation zones (Huang and Johnson 2010), the ratios of hanging wall to footwall deformation zone width for strike-slip faults are 6, 3, and 1 for fault angles of 45°, 60° and 90°, respectively. We have discovered that the Chihshang main fault at Tapo ES is located about 55 m from the toe of the escarpment to the east and juxtaposes the alluvium deposit and the Lichi mélange with a dip angle of approximately 77°. We further compared the whereabouts of the Chihshang main fault with the leveling measurements of Yu and Liu (1989). There was an abrupt change in relative vertical displacement between BM1014 and BM792 for the period March 1987 to May 1988 (Fig. 2). The projected distances in the direction perpendicular to the ChF are approximately 71.2 m and 95.6 m in reference to BM057, respectively. BM057 is located approximately 37.1 m west of the escarpment toe at Tapo ES (Fig. 1). Therefore, the abrupt change in relative vertical displacement happened between 34.1 m and 58.5 m east of the escarpment. This indicated that a creeping fault is located somewhere in this range and strongly supports our findings in terms of fault position and activity. Most studies on the ChF, e.g., Mu et al. (2011) and Chu (2007), have presumed that the abrupt change in slope steepness at the hill front is the morphologic expression of the Chihshang main fault. With additional subsurface information, they inferred that the fault has an intermediate dip angle ranging from 35° to 45°. In contrast, the relevant trenches excavated at the sites of abrupt change in slope steepness at the hill front showed no sign of Lichi Mélange or deformation (Chu 2007). Such observations imply that these sites are likely not where the main fault reaches the surface. Similar to our result, Chen (2008) reported that the Chihshang main fault has a dip angle of at least 65° in Wanan based on the positions of the fault in two boreholes (Fig. 2c) and this outcome matched the direct measurement of the fault angle of 67° on the core. He also indicated that the surface trace of the Chihshang main fault is located on the hillside. Based on his data, we inferred that the fault trace is located on the slope at least a couple of decameters away from the toe of the slope (Fig. 2d). In addition, the outcrop of the ChF on the Bieh river bank in Fuli earlier mentioned (Fig. 2b) has been reported to have a dip of 60° ESE (Barrier and Chu 1984). This outcrop is particularly interesting because the fault truncates a Holocene river terrace. The terrace gravel is on top of the Lichi Mélange with a height of 25 m above the Bieh riverbed in the hanging wall while the terrace gravel is on top of the Pleistocene conglomerate 10 m above the riverbed in the footwall (Chen 1993). Obviously, the trace of the main fault is not located at the western edge of the terrace gravel where there is a topographic relief. It is worth mentioning that there was an *M*5.4 earthquake rupture extending 6 km with successive fractures in the hillside in this region in 1992 (Yu et al. 1994). So far, there is significant evidence to suggest that the Chihshang main fault has a high dip angle of 60° or even higher at depth ranging from a few meters to likely hundreds of meters. However, this does not contradict the observations of thrust or intermediate angle reverse faults in man-made structures or unconsolidated sediment layers in Chinyuan (Mu et al. 2011; Angelier et al. 1997; Chu et al. 1994) because those faults are likely splay branches of the main fault or induced by the splay faults or the main fault. But, why is the ChF angle of 77° in Tapo higher than those in other places, ranging from 60° to 67° at shallow depths and 60° at a depth of 5 km inferred from relocated seismicity? It might result from higher pure shear in Tapo. Or, the lateral variation of the fault geometry resulted from heterogeneous materials in the Lichi mélange. Both of our explanations are speculative; further studies are needed to confirm.

Before further discussing the location of its surface trace, we need to emphasize that the ChF is most likely a zonal structure with thickness ranging from a few meters to hundreds of meters and our above discussion has mainly focused on the main fault which is the contact of the Lichi mélange and Quaternary sediment. We have shown several cases where the projected locations of the main fault on ground surface are not in the toe of topographic slope. In our opinion, the hill front with abrupt change in the slope is mostly not where the Chihshang main fault is located. However, we also noticed that agricultural activities and road cuts have shaped the toe of the slope. This is in addition to the complexity of a longstanding fault in terms of along-fault variations in fault geometry and surface deformation. Therefore, it may be more correct to state that the topographic relief at the toe of the western side of the coastal range in this region is the ChF-line scarp instead of fault scarp (Fairbridge 1968). The fault-line scarp at Tapo ES was analyzed to demonstrate how it evolved, as discussed in sub Sect. 5.3.

5.1.2 Frontal deformation mechanism at Tapo ES

We observed a gradation zone in the ERT profiles and discovered that it was relevant to the mixed zone of the Chihshang main fault. Based on data from the inclinometer installed in borehole TP-8, the main fault had ongoing aseismic slip or, in other words, deformation. Its 2-year cumulative displacement of 20.7 mm was northwestward with a N–S component value of 8.6 mm/year and a W–E component value of 5.8 mm/year. Assuming that the displacement occurred in the fault zone striking N18°E, the N–S and W–E components could have been transformed into left-lateral slip rate of 8.2 mm/year and transverse slip rate of 6.4 mm/year. However, the cumulative displacement of 35.2 mm is northwest-northward as recorded by the inclinometer installed in the borehole of TP-7 and shows a N–S component value of 17.3 mm/year, was almost 5 times greater than the W–E component value of 3.1 mm/year. Under the same assumption, these can be transformed into left-lateral slip rate of 15.5 mm/year and transverse slip rate of 8.3 mm/year. These two component values were much higher than their counterparts in TP-8. We can reasonably attribute this to the change in fault angle, which is 77° in TP-8 and only a few degrees in TP-7 (Fig. 14). Due to the change in fault angle, the vertical component of the fault slip in TP-8 likely contributed to the increase in the N–S component and W–E component of the fault slip in TP-7 because the hanging-wall mudstone of the mélange was raised to a higher potential-energy place with westward spread by gravity. Furthermore, based on the current observations at the toe of the slope abutting the Tapo ES, along with the shortening of 16 mm/

year derived from creepmeters by Lee et al. (2003), the transverse component was dominant and WNW to ESE. This shortening was almost twice as much as the transverse slip rate in TP-7. Note that there was a retaining wall blocking the downward mass at the toe of the slope. Therefore, besides faulting, there must be other mechanisms resulting in this frontal deformation. We have noted earlier that there is a slipping plane between the in situ mélange and reworked mélange at shallow depth in TP-7 and TP-6. Likely, this slipping plane extended downwards and connected with the fault contact beneath the escarpment reported by Chu et al. (1988). It formed a west-dipping basal sliding surface. The location of its upper edge may correspond to the steepest section of the frontal slope in between TP-6 and TP-7B (Fig. 14). Furthermore, Chang et al. (2003) reported a north–south-trending extensional fissure with an opening width of 15 cm and a length of at least a few meters on this slope. The intense frontal deformation may be largely attributed to the gravity driven deformation above this basal surface; that is landsliding. This mechanism is most likely gravity gliding (Schultz-Ela 2001). In contrast, the aseismic slip along the high-angle ChF at this site is likely attributed to the constant tectonic loading of the collision between Eurasian plate and Philippine Sea plate with relative convergence at a rate of about 82 mm/year (Yu et al. 1997 and 1999). This not only contributes partial shortening, but also translates the mudstone of Lichi mélange to the higher ground surface so that landsliding can follow up. That is to say, the uplifted mass of the mudstone subsequently slides down along the west-dipping basal surface. Thus, we coined the term "faulting-relay landsliding" for faulting and landsliding in tandem that produced the deformation on the escarpment at Tapo ES. Our finding also implies that great caution is needed for interpreting aseismic surface ruptures along the inferred trace of the ChF (Jiang et al. 2012) as fault branching.

5.2 How is the ChF slip transferred from the earthquake source to the surface?

Huang et al. (2010) inverted inter-seismic surface displacements and Holocene marine terrace data for fault slip rates and distribution of inter-seismic creep, based on a model of elastic lithospheric blocks moving over a viscoelastic asthenosphere in eastern Taiwan. Their results showed that the ChF creeps at a rate of 5–28 mm/year down to a depth of 15–20 km and the rate increases towards the ground surface. Based on the 1999–2001 monitoring results of three creepmeters straddled on three branch fault traces in Chinyuan (location shown in Fig. 3) there is merging into a main fault at deeper depth (Mu et.al., 2011). Lee et al. (2003) indicated that the ChF has an annual horizontal shortening rate of 15.0 mm/year with seasonal variation: rapid shortening during the wet season and slow shortening during the dry season. Two creepmeters that straddle the retaining wall were installed in 1998 perpendicular to the trace of the scarp to monitor gradual motion in the ChF zone at Tapo ES. Lee et al. (2003) indicated that the average rate of annual shortening at this site is 16.2 mm/year derived from these two creepmeters during the period 1999 to 2001 and this shortening rate is consistent with that at the Chinyuan site described above. They also pointed out that the result from one of the two creepmeters showed seasonal variation while the other showed shortening regardless the season and abrupt pulse of displacement at least once per year. Lee et al. (2003) suggested that the sudden displacements can be attributed to rotation of one of the piers supporting the creepmeter by a minor landslide.

Our inclinometer was installed at depths of 21.3 to 31.3 m of TP-8 and penetrated the Chihshang main fault. It showed continuous movement of the main fault during its operating duration. The inclinometer was also installed at depths of 5 to 15 m of TP-7 and penetrated one or two inferred flat fault branches. It also showed continuous movement of the branches. Therefore, we examined those segments of the inclinometer with larger displacement to confirm whether their deformation has comparable pattern related to rainfall variation. However, after thorough examination, we did not notice any seasonal deformation pattern or pattern associated with rainfall. Examples are shown in Fig. 11b. The 2-year cumulative deformation for the most active segment of each borehole compared to the contemporary cumulative rainfall is shown in Fig. 11c. Our observations differ from those of Lee et al. (2003) in terms of seasonal variation. One reasonable explanation is that those fault branches on which the creepmeters were straddled are within alluvial deposits at the shallow surface and their behavior might be affected by rainfall, unlike the segments with larger displacement in our inclinometer at certain depths with the clay-rich Lichi Mélange. Namely, the material property controls the behavior of the fault creep at different depths. Likely, at the area covered by a thick sediment layer, the fault persistently creeps at depth but its slip converts to strain energy in the thick sediment layer while it approaches to the ground surface. Therefore, the branches of the fault on the ground which were reported by Lee et al. (2003) were dormant in dry seasons. Until wet seasons, they would be mobilized by the precipitation and reactivate. As mentioned above, its 2-year cumulative displacement of 20.7 mm northwestward can be transformed into left-lateral slip rate of 8.2 mm/year and transverse slip rate of 6.4 mm/

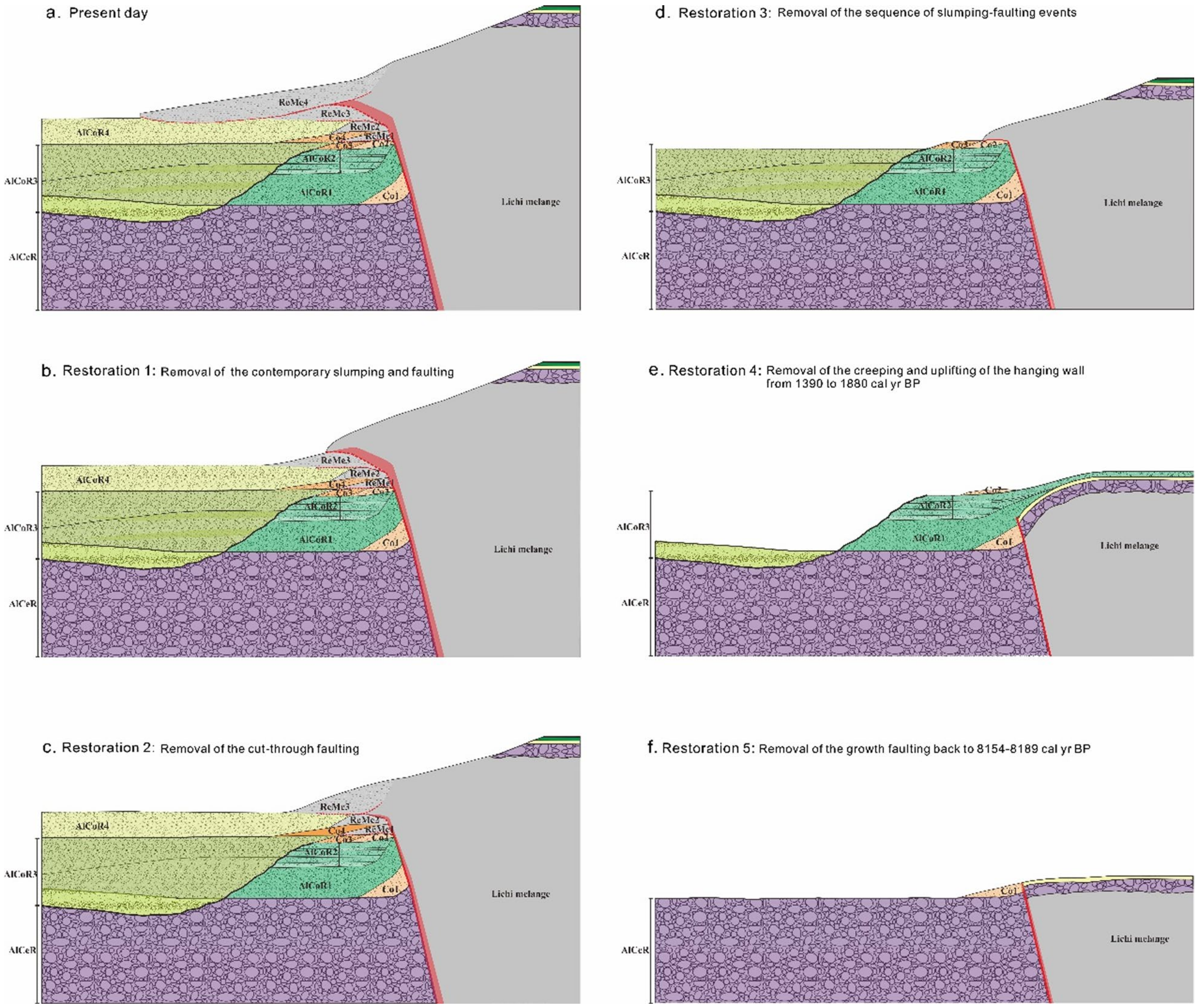

Fig. 15 Reconstruction of the ChF evolution related to the escarpment at Tapo ES. The restoration shows progressive unstripping of stratigraphy and removal of deformation. The red bold line indicates the ChF

year. Assuming that the fault dip is 77°, the fault slip can be derived as 29.6 mm/year. This value is comparable to the fault slip of 28 mm/year predicted by Huang et al. (2010). Thus, we conclude that the ChF continuously creeps without seasonal variation and branches out at shallow depths.

5.3 Holocene evolution of Chihshang creeping fault-line scarp

We inferred the evolution of the Chihshang creeping fault-line scarp and restored the fault movement from the present status backwards (Fig. 15). The trishear fault-propagation folding (Erslev 1991; Hardy and Ford 1997) may be explained by the folded growth strata in the footwall and different locations of the subsurface branches of the main fault. However, unlike structures and folded growth strata fully exposed on excavated trenches (e.g., Lin et al. 2007), our subsurface structure was constructed based on limited observations so that we simply performed each restoration based on the law of superposition and the principle of crosscutting relations. In the present day, we have the subsurface structure model that we concluded in the previous section. In this stage, the major escarpment corresponded to the front of the reworked mélange, labeled as ReMe4.

In restoration 1, we undid the ReMe4, the youngest reworked mélange settlement, which was the result of the combination effect of gravity sliding and faulting. In this stage, the escarpment was represented as the upper tip of the main fault. In restoration 2, we undid the cut-through faulting. In this stage, the fault reached the ground surface and the mudstone of the Lichi mélange creeping along the ground surface. In restoration 3, we undid a sequence of creep events. At this stage, the tongue of the Lichi Mélange was lying above the colluvial deposit, Co2, with settlement of the colluvial deposit, Co3. In restoration 4, we undid the uplifting of the hanging wall, from 1390 to 1880 cal yr BP. In this stage, significant scouring occurred in the footwall and settlement of alluvium, AlCoR3, and colluvial deposit, Co2, proceeded. In restoration 5, we undid the growth faulting. In this furthest restoration that we can infer, all units that overlay the alluvium sourced from Central Range were removed except colluvial deposit, Co1. In the last stage, the surface was covered by slope wash from the hillside in the east; however, the fault cut through this layer and generated colluvial deposit, Co1 on the surface. Note that the uplift rate might change and be not consistent with the modern uplift rate of approximately 1.8 cm/year based on leveling data as forementioned earlier. This illustrative evolution in Fig. 15 shows us that the western leading frontal slope of the Coastal Range in Tapo resulted from the trio of faulting, fluviation, and landsliding.

As mentioned earlier, the geomorphic scarp bounding the eastern side of the Longitudinal Valley is commonly regarded as the first-order location for the trace of the ChF and even the LVF (Shyu et al. 2006). Great caution is required when using such an escarpment to locate the LVF in the Coastal Range, in particular, where the Lichi Mélange is distributed widely in the south. For example, in Wanan (shown in Fig. 2), two trenches were dug across the toes of the geomorphic scarp in 2006 (Chen et al. 2006; Chu 2007; Yen et al. 2014) and three boreholes were drilled in 2007 following a line perpendicular to the strike of the ChF (Chen 2008). One trench showed that sediments were cut by 7 minor faults with different vertical displacements up to 65 cm while in the other trench monoclinal sediment layers were exposed without any fracture. The three boreholes were apparently located in the hanging wall of the ChF. Two of them penetrated the ChF and revealed the fault angle to be 65° (Fig. 2d). The easternmost third borehole did not penetrate through the Lichi Mélange. Based on these observations, Chen (2008) concluded that the ChF trace was located (at least 10 m) on the topographic slope east of the two trenches and the deformation features in the trenches likely resulted from the topographic effect at the escarpment toe. Another example that involved a test reactor near Livermore, California, has led to an unsettled debate on whether a kilometer-scale arcuate scarp is the toe of a landside or the Verona Fault (Hart et al. 2012). After thoroughly examining all studies on the case, Hart et al. (2012) pointed out that large landslides and faults can occupy the same space and suggested that landsides may be triggered by nearby fault activity and may use fault planes as failure surfaces. Our Tapo case clearly demonstrated this inference and may serve as one classic type of frontal deformation of reverse faults. Those who tackle frontal deformation may be reminded of not only creeping reverse faults, but also creeping thrust faults, such as the northern rangefront fault of high Tien Shan, Kazakhstan (Mackenzie et al. 2018).

6 Conclusions

We constructed the subsurface structural configuration in Tapo ES area based on multidisciplinary data: 2D resistivity inversion of ERT, rock cores of seven boreholes, dating, and inclinometer monitoring. The western frontal slope of the Coastal Range is approximately 25 m high with a flat hilltop capped by 1.5-m-thick alluvium sediments and a roughly 1.5-m-high escarpment at its toe in this area. The retaining wall and facilities sustained deformation and damage at and on the escarpment. Based on an integrated result from an inverted-resistivity model and rock cores, the high-resistivity domain (>30 Ω-m) to the west corresponded with the alluvium deposits, while the low-resistivity domain (<10 Ω-m) to the east corresponded with the mudstone of Lichi Mélange. The Chihshang main fault was found as the contact of these two lithologic units with a dip angle of approximately 77° within the resistivity gradation zone 55 m east of the toe of morphologic escarpment.

The inclinometer recorded active displacements on the fault contact and its branches, and much greater N–S component of horizontal displacements in both TP-7 and TP-8, which explicitly indicates the main contribution of ChFing with the left-lateral sense. The 2-year cumulative horizontal displacement was 20.7 mm northwestward and can be transformed into the left-lateral slip rate of 8.2 mm/year and transverse slip rate of 6.4 mm/year. The deformation shows no comparable pattern related to rainfall variation. On the contrary, the transverse deformation was dominant on the escarpment. On the basis of field and core observations, the mélange-related material with non-sheared irregular texture was distributed from the fault tip to the escarpment toe. From this, we conclude that active deformation on the escarpment at Tapo ES results from gravity sliding of the mass which is steadily supplied by Chihshang faulting. A mechanism of faulting-relay landsliding is proposed to apprehend the active deformation on the escarpment. Thus, the trio of faulting, fluviation and landsliding resulted in this frontal slope in Tapo. This implies that great caution should be taken when inferring that aseismic surface ruptures along plausible trace of reverse creeping faults are indicative of fault branching.

Acknowledgements
This research was supported by the Geological Survey and Mining Management Agency and Taiwan Ministry of Science and Technology (MOST 108-2116-M-008-020). Readers are welcome to contact the corresponding author for any inquiry regarding the present study.

Author contributions
1. Wen-Jeng Huang: Conceptualization Methodology Validation Formal Analysis Investigation Data Curation Writing - Original Draft Writing - Review and Editing Supervision. 2. Mohammad Tri Fitrianto: Formal Analysis Investigation Data Curation Writing - Original Draft. 3. Chien-Chih Chen: Conceptualization Methodology Writing - Original Draft Writing - Review and Editing. 4. Ping-Yu Chang: Conceptualization Methodology Supervision. 5. I-Chin Yen: Investigation Data Curation. 6. Maryline Le Béon: Writing - Review and Editing. 7.Shih-Ting Lu:Methodology Supervision. All authors have approved the final version of this manuscript.

Availability of data and materials
Derived data from this study and raw data used in this study, including resistance data, inclinometer displacements, and daily rainfall are in Mendeley Data repository. ERT data (i.e., resistance data) are available at https://dx.doi.org/https://doi.org/10.17632/7z9y5rxcmz.1 (Huang and Chen 2023). The raw data and derived daily averages of inclinometer displacements are available at https://dx.doi.org/https://doi.org/10.17632/wn44yw9465.1 (Huang 2023a). The data of daily rainfall are available at https://dx.doi.org/https://doi.org/10.17632/7rpnpjvk7b.1 (Huang 2023b).

Competing interests
The authors declare that they have no competing interests.

Author details
[1]Graduate Institute of Applied Geology, National Central University, No. 300, Jhongda Rd., Jhongli, Taoyuan 32001, Taiwan. [2]Department of Earth Sciences, National Central University, No. 300, Jhongda Rd., Jhongli, Taoyuan 32001, Taiwan. [3]Earthquake-Disaster & Risk Evaluation and Management Center, National Central University, No. 300, Jhongda Rd., Jhongli, Taoyuan 32001, Taiwan. [4]Yic Geologist Office, Taipei, Taiwan. [5]Geological Survey and Mining Management Agency, MOEA, No. 2, Ln. 109, Huaxin St., Zhonghe, New Taipei 235, Taiwan.

Received: 13 September 2024 Accepted: 31 December 2024

References

Abdoun T, Bennett V, Danisch L, Shantz T, Jang D (2007) Field installation details of a wireless shape-acceleration array system for geotechnical applications. Proc SPIE 6529(65293O):1–10. https://doi.org/10.1117/12.714413

Agalianos A, De Caudron de Coquereaumont, O Anastasopoulos I, 2019. Strike–slip fault rupture propagation through sand and interaction with slab foundations. In: Online Proc. 2nd Int. Conf. Nat. Hazards Infrastruct. (ICONHIC 2019), 255.

AGI 2009. Instruction Manual for EarthImager 2D Version 2.4.0, Austin, Texas: Advanced Geosciences, Inc.

Anastasopoulos I, Gazetas G (2007) Foundation-structure systems over a rupturing normal fault: part I. observations after the Kocaeli 1999 earthquake. Bull Earthq Eng 5:253–275. https://doi.org/10.1007/s10518-007-9029-2

Angelier J, Barrier E, Chu HT (1986) Paleostress trajectories related to plate collision in the foothills fold-thrust belt of Taiwan. Memoir Geol Soc China 7:201–217

Angelier J, Chu HT, Lee JC (1997) Shear concentration in a collision zone: kinematics of the Chihshang fault as revealed by outcrop-scale quantification of active faulting, Longitudinal Valley, eastern Taiwan. Tectonophysics 274:117–143. https://doi.org/10.1016/S0040-1951(96)00301-0

Angelier J, Chu HT, Lee JC, Hu JC (2000) Active faulting and earthquake hazard: the case study of the Chihshang Fault Taiwan. J Geodynamics 29:151–185. https://doi.org/10.1016/S0264-3707(99)00045-9

Barrier E, Chu HT, 1984. Field trip guide to the Longitudinal Valley and Coastal Range in eastern Taiwan. Field Guidebook, Sino-French Colloquium on Geodynamics of the Eurasian-Philippine Sea Plate Boundary, 27–49.

Biq CC (1972) Dual-trench structure in the Taiwan-Luzon region. Proc Geol Soc China 15:65–75

Bird JF, Bommer JJ (2004) Earthquake losses due to ground failure. Eng Geol 75:147–179. https://doi.org/10.1016/j.enggeo.2004.05.006

Chai BHT (1972) Structure and tectonic evolution of Taiwan. Am J Sci 272:389–422. https://doi.org/10.2475/ajs.272.5.389

Champenois J, Fruneau B, Pathier E, Deffontaines B, Lin KC, Hu JC (2012) Monitoring of active tectonic deformations in the longitudinal valley (eastern Taiwan) using persistent scatterer InSAR method with ALOS PALSAR data. Earth Planet Sci Lett 337:144–155

Chang CP, Angelier J, Huang CY (2000) Origin and evolution of mélange: the active plate boundary and suture zone of the Longitudinal Valley. Taiwan Tectonophysics 325:43–62. https://doi.org/10.1016/S0040-1951(00)00130-X

Chang CP, Angelier J, Huang CY, Liu CS (2001) Structural evolution and significance of a mélange in a collision belt: the Lichi Mélange and the Taiwan arc-continent collision. Geol Magazine 138(6):633–651. https://doi.org/10.1017/S0016756801005970

Chang CP, Chang TY, Liu C, Lee JC, Tsai YB, Jian KC, Huang SJ, Wu SW (2003) Surface deformation and mechanisms in the Chihshang Area, longitudinal Valley of Taiwan. Spec Public Cent Geol Survey 14:203–214

Chang YY, Lee WC, Huang WC, Hung WY, Huang WJ, Lin ML, Chen YH (2015) Evolution of the surface deformation profile and subsurface distortion zone during reverse faulting through overburden sand. Eng Geol 184:52–70

Chang PY, Huang WJ, Chen CC, Hsu HI, Yen IC, Ho GR et al (2018) Probing the frontal deformation zone of the Chihshang Fault with boreholes and high-resolution electrical resistivity imaging methods: a case study at the Dapo site in eastern Taiwan. J Appl Geophys 153:127–135. https://doi.org/10.1016/j.jappgeo.2018.04.006

Chen WS (1993) Consideration on the activity of the longitudinal valley fault, in the Coastal Range. Sino-Geotechnics 44:52–57

Chen WS (1997) Lithofacies analyses of the arc-related sequence in Coastal Range, eastern Taiwan. J Geol Soc China 40(2):313–338

Chen WS (2008) Study on long-term slip rate and recurrence interval of faults. Rep Taiwan Cent Geol Survey 97(9):31–40

Chen HH, Rau RJ (2002) Earthquake locations and style of faulting in an active arc-continent plate boundary: The Chihshang fault of eastern Taiwan. Eos Trans AGU 83:47

Chen WS, Wang Y (1988) The plio-pleistocene basin development in the coastal range of Taiwan. Acta Geol Taiwan 26:37–56

Chen HY, Yu SB, Kuo LC, Liu CC (2006) Coseismic and postseismic surface displacement of the 10 December 2003 (Mw 6.5), eastern Taiwan, earthquake. Earth Planet and Space 58:5–21. https://doi.org/10.1186/BF03351908

Chen WS, Yen IC, Fengler KP, Rubin CM, Yang CC, Yang HC, Chang HC, Lin CW, Lin WH, Liu YC, Lin YH (2007) Later Holocene paleoearthquake activity in the middle part of the Longitudinal Valley fault, eastern Taiwan. Earth Planet Sci Lett 264:420–437

Cheng SN, Yeh YT, Yu MS (1996) The 1951 Taitung earthquake in Taiwan. J Geol Soc China 39(3):267–285

Chu YK (2007) Paleoseismology of the Chihshang Fault. National Taiwan University. https://doi.org/10.6342/NTU.2007.02908

Chu HT, Lee JC, Angelier J (1994) Non-seismic rupture of the Tapo and Chiyuan area on the southern segment of Huatung Longitudinal Valley Fault Eastern Taiwan. Annual Meeting of Soc Geol China Taipei 1:5

Chu HT, Angelier J, Lee JC, 1988. Field trip guide to the active Chihshang Fault: A non-seismic rupture of the Tapo and the Chinyuan area on the southern segment of the Longitudinal Valley Fault, eastern Taiwan. In H. T. Chu, J. C. Lee (Eds). Field Guidebook of Western Pacific Geophysics Meeting (pp. 1–11).

Erslev EA (1991) Trishear fault-propagation folding. Geology 19:617–620

Faccioli E, Anastasopoulos I, Gazetas G, Callerio A, Paolucci R (2008) Fault rupture-foundation interaction: selected case histories. Bull Earthq Eng 6:557–583. https://doi.org/10.1007/s10518-008-9089-y

Fadaee M, Hashemi K, Farzaneganpour F, Anastasopoulos I, Gazetas G (2020) 3-storey building subjected to reverse faulting: analysis and experiments.

Soil Dyn Earthq Eng 138:106297. https://doi.org/10.1016/j.soildyn.2020.106297

Fairbridge RW (1968) Fault scarp, fault-line scarp. Encyclopedia Earth Sci. https://doi.org/10.1007/3-540-31060-6_125

Fitrianto MT, 2020. Characteristics of the Chihshang fault at Tapo elementary school area, Eastern Taiwan, (Master's thesis), pp.122. (https://hdl.handle.net/11296/de6a8k). National Central University, Taiwan.

Garcia FE, Bray JD (2019a) Discrete-element analysis of influence of granular soil density on earthquake surface fault rupture interaction with rigid foundations. J Geotechn Geoenviron Eng 145:04019093. https://doi.org/10.1061/(ASCE)GT.1943-5606.0002163

Garcia FE, Bray JD (2019b) Discrete element analysis of earthquake fault rupture soil-foundation interaction. J Geotechn Geoenviron Eng 145:04019046. https://doi.org/10.1061/(ASCE)GT.1943-5606.0002092

Hardy S, Ford M (1997) Numerical modeling of trishear fault propagation folding. Tectonics 16(5):841–854. https://doi.org/10.1029/97tc01171

Hart MW, Shaller PJ, Farrand GT (2012) When landslides are misinterpreted as faults: Case Studies from the Western United States. Environ Eng Geosci 18(4):313–325

Ho CS (1986) A synthesis of the geologic evolution of Taiwan. Tectonophysics 125:1–16. https://doi.org/10.1016/0040-1951(86)90004-1

Hsu TL (1962) Recent faulting in the longitudinal valley of Eastern Taiwan. Memoir Geol Soc China 1:95–102

Hsu YJ, Lai YR, You RJ, Chen HY, Teng LS, Tsai YC et al (2018) Detecting rock uplift across southern Taiwan mountain belt by integrated GPS and leveling data. Tectonophysics 744:275–284. https://doi.org/10.1016/j.tecto.2018.07.012

Hu JC, Cheng LW, Chen HY, Wu YM, Lee JC, Chen YG et al (2007) Coseismic deformation revealed by inversion of strong motion and GPS data: the 2003 Chengkung earthquake in eastern Taiwan. Geophys J Int 169:667–674. https://doi.org/10.1111/j.1365-246X.2007.03359.x

Huang WJ (2023a) Inclinometer displacement. National Central University. https://doi.org/10.17632/wn44yw9465.1

Huang WJ (2023b) Daily Rainfall data from 1 July 2016 to 30 June 2018 and from 1 Jan 2019 to 31 Dec 2020. National Central University. https://doi.org/10.17632/7rpnpjvk7b.1

Huang WJ, Chen CC (2023) ERT data for the survey at Tapo ES, eastern Taiwan. National Central University. https://doi.org/10.17632/7z9y5rxcmz.1

Huang WJ, Johnson AM (2010) Quantitative description and analysis of earthquake-induced deformation zones along strike-slip and dip-slip faults. J Geophys Res 115:B03408. https://doi.org/10.1029/2009JB006361

Huang WJ, Johnson KM, Fukuda J, Yu SB (2010) Insights into active tectonics of eastern Taiwan from analyses of geodetic and geologic data. J Geophys Res 115:B03413. https://doi.org/10.1029/2008JB006208

Huang, W.J., 2006, Deformation at the leading edge of thrust faults, Ph.D. dissertation, pp. 435, Purdue Univ., West Lafayette, Indiana, July.

Improta L, Ferranti L, De Martini PM, Piscitelli S, Bruno PP, Burrato P, Civico R, Giocoli A, Iorio M, D'Addezio G, Maschio L (2010) Detecting young, slow-slipping active faults by geologic and multidisciplinary high-resolution geophysical investigations: a case study from the Apennine seismic belt, Italy. J Geophys Res 115:B11307. https://doi.org/10.1029/2010JB000871

Jiang YL, Chu HT, Lee JC, Huang CY (2012) Investigation and characterization of surface ruptures and deformation zone of the Chihshang fault, eastern Taiwan. Spec Public Centl Geol Survey 26:101–138

Johnson AM, Johnson KM, Durdella J, Sözen M, Gür T (2002) An emendation of elastic rebound theory: Main rupture and adjacent belt of right-lateral distortion detected by viaduct at Kaynasli, Turkey 12 November 1999 Duzce earthquake. J Seismolog 6:329–346. https://doi.org/10.1023/A:1020031324622

Kim KH, Chiu JM, Pujol J, Chen KC, Huang BS, Yeh YH, Shen P (2005) Three-dimensional Vp and Vs structural models associated with the active subduction and collision tectonics in the Taiwan region. Geophys J Int 162:204–220

Konagai K (2005) Data archives of seismic fault-induced damage. Soil Dyn Earthq Eng 25:559–570

Lawson AC (1908) California earthquake of April 18, 1906: report of the state earthquake investigations commission. Carnegie Inst Washington Publ 87(1):451

Lazarte CA, Bray JD, Johnson AM, Lemmer RE (1994) Surface breakage of the 1992 Landers earthquake and its effects on structures. Bull Seismol Soc Am 84(3):547–561

Lee JC, Jeng FS, Chu HT, Angelier J, Hu JC (2000) A rod-type creepmeter for measurement of displacement in active fault zone. Earth Planets Space 52:321–328

Lee JC, Angelier J, Chu HT, Hu JC, Jeng FS (2001) Continuous monitoring of an active fault in a plate suture zone: a creepmeter study of the Chihshang Fault, eastern Taiwan. Tectonophysics 333:219–240

Lee JC, Angelier J, Chu HT, Hu JC, Jeng FS, Rau RJ (2003) Active fault creep variations at Chihshang, Taiwan, revealed by creep meter monitoring, 1998–2001. J Geophys Res 108(B11):2528. https://doi.org/10.1029/2003JB002394

Lee JC, Chu HT, Angelier J, Hu JC, Chen HY, Yu SB (2006) Quantitative analysis of surface coseismic faulting and postseismic creep accompanying the 2003, Mw = 6.5, Chengkung earthquake in eastern Taiwan. J Geophys Res 111:B02405. https://doi.org/10.1029/2005JB003612

Lee YH, Chen GT, Rau RJ, Ching KE (2008) Coseismic displacement and tectonic implication of 1951 Longitudinal Valley earthquake sequence, eastern Taiwan. J Geophys Res 113:B04305. https://doi.org/10.1029/2007JB005180

Li CH, Lin ML, Huang WC (2019) Interaction between pile groups and thrust faults in a physical sandbox and numerical analysis. Eng Geol 252:65–77. https://doi.org/10.1016/j.enggeo.2019.02.023

Lin AT, Watts AB, Hesselbo SP (2003) Cenozoic stratigraphy and subsidence history of the South China See margin in the Taiwan region. Basin Res 15:453–478. https://doi.org/10.1046/j.1365-2117.2003.00215.x

Lin ML, Wang CP, Chen WS, Yang CN, Jeng FS (2007) Inference of trishear-faulting processes from deformed pregrowth and growth strata. J Struct Geol 29(7):1267–1280. https://doi.org/10.1016/j.jsg.2007.03.017

Lin CW, Chen WS, Liu YC, Chen PT (2009) Active faults of eastern and southern Taiwan. Spec Public Centl Geol Survey 23:178

Lin ML, Lin CH, Li CH, Liu CY, Hung CH (2021) 3D modeling of the ground deformation along the fault rupture and its impact on engineering structures: insights from the 1999 Chi-Chi earthquake, Shigang District. Taiwan Eng Geol 282:105993. https://doi.org/10.1016/j.enggeo.2021.105993

Lin CW, Chang HC, Lu ST, Shih TS, Huang WJ, 2000. An Introduction to the Active Faults of Taiwan. Special publication of the Central Geological Survey 13.

Liu CY, Li CH, Chan PC, Hung CH, Lin ML (2020) 3D physical and numerical modeling of coseismic surface rupture induced by oblique-slip faulting and its interaction with embedded shallow foundation. Eng Geol 282:105990. https://doi.org/10.1016/j.enggeo.2021.105990

Mackenzie D, Walker R, Abdrakhmatov K, Campbell G, Carr A, Cruetzner C, Mukambayev A, Rizza M (2018) A creeping intracontinental thrust fault: past and present slip-rates on the Northern edge of the Tien Shan, Kazakhstan. Geophys J Int 215:1148–1170. https://doi.org/10.1093/gji/ggy339

McCalpin JP, Carver GA (2009) Paleoseismology of compressional tectonic environments. Int Geophys 95:327–330. https://doi.org/10.1016/S0074-6142(09)95005-7

Measurand Inc., a technology company specializing in fiber-optic and other measuring systems. http://www.measurand.com Accessed 7 October 2021.

Mu CH, Angelier J, Lee JC, Chu HT, Dong JJ (2011) Structure and Holocene evolution of an active creeping thrust fault: the Chihshang fault at Chinyuan (Taiwan). J Struct Geol 33(4):743–755. https://doi.org/10.1016/j.jsg.2011.01.015

Nabi A, Liu XD, Gong Z, Ali A (2020) Electrical resistivity imaging of active faults in palaeoseismology: case studies from Karachi Arc, southern Kirthar Fold Belt Pakistan. NRIAG J Astronomy Geophys 9(1):116–128. https://doi.org/10.1080/20909977.2020.1722524

Ng SM, Angelier J, Chang CP (2009) Earthquake cycle in Western Taiwan: Insights from historical seismicity. Geophys J Int 178(2):753–774. https://doi.org/10.1111/j.1365-246X.2009.04164.x

Pamuk A, Kalkan E, Ling HI (2005) Structural and geotechnical impacts of surface rupture on highway structures during recent earthquakes in Turkey. Soil Dyn Earthq Eng 25:581–589. https://doi.org/10.1016/j.soildyn.2004.11.011

Reid, H.F., 1910. Report of the State Earthquake Investigation Commission, II: The mechanics of the earthquake Carnegie Inst. of Washington. Washington, D. C.

Rowe CD, Lamothe K, Rempe M, Andrews M, Mitchell TM, Di Toro G et al (2019) Earthquake lubrication and healing explained by amorphous nanosilica. Nat Commun 10(1):320. https://doi.org/10.1038/s41467-018-08238-y
Schultz-Ela DD (2001) Excursus on gravity gliding and gravity spreading. J Struct Geol 23:725–731
Shin TC, Chang ZS (1992) Earthquake in 1992. Meteorol Bull 38(3):218–232
Shyu JBH, Chung LH, Chen YG, Lee JC, Sieh K (2006) Re-evaluation of the surface ruptures of the November 1951 earthquake series in eastern Taiwan, and its neotectonics implications. J Asian Earth Sci 31(3):317–331. https://doi.org/10.1016/j.jseaes.2006.07.018
Sibson RH (1977) Fault rocks and fault mechanisms. J Geol Soc 133:191–213. https://doi.org/10.1144/gsjgs.133.3.0191
Steinbrugge KV, Schader EE, Moran DF (1973) Building damage in San Fernando valley, in San Fernando, California, earthquake of 9 February 1971, edited by G. Oakeshott. Calif Div Minesgeol Bull 196:323–368
Taiwan Central Geological Survey, 2000. Geologic Map of Taiwan, map at scale, 1:500000, Central Geol. Surv., Minist. of Econ. Affairs, Taipei.
Teng LS (1987) Tectonostratigraphic facies and geologic evolution of the Coastal Range, eastern Taiwan. Memoir Geol Soc China 8:229–250
Thomas MY, Avouac JP, Gratier JP, Lee JC (2014) Lithological control on the deformation mechanism and the mode of fault slip on the longitudinal valley fault. Taiwan Tectonophysics 632:48–63
Tsai YB (1985) A study of disastrous earthquakes in Taiwan, 1683–1895. Bull. Inst. Earth Sc. Acad Sin 5:1–44
Wu F (1978) Recent tectonics in Taiwan. J Phys Earth 26:265-S299
Wu YM, Chen YG, Shin TC, Kuochen H, Hou CS, Huo JC, Chang CH, Wu CF, Teng TL (2006) Coseismic versus interseismic ground deformations, fault rupture inversion and segmentation revealed by 2003 Mw 68 Chengkung earthquake in eastern Taiwan. Geophys Res Lett 33:L02312. https://doi.org/10.1029/2005GL024711
Wu WJ, Kuo LW, Ku CS, Chiang CY, Sheu HS, Aprilniadi TD, Dong JJ (2020) Mixed-mode formation of amorphous materials in the creeping zone of the Chihshang Fault, Taiwan, and implications for deformation style. J Geophys Res Solid Earth. https://doi.org/10.1029/2020JB019862
Yang S, Mavroeidis GP (2018) Bridges crossing fault rupture zones: a review. Soil Dyn Earthq Eng. https://doi.org/10.1016/j.soildyn.2018.03.027
Yen IC, Chen WS, Sung SH, Huang NW, Yang CC, Liu YC, Lin CW (2014) Paleoseismological study on the Chihshang segment of the longitudinal valley fault in eastern Taiwan. Spec Public Centl Geol Survey 28:43–70
Yu SB, Kuo LC (1999) GPS observation of crustal deformation in the Taiwan-Luzon. Geophys Res Lett 26(7):923–926
Yu SB, Kuo LC (2001) Present-day crustal motion along the Longitudinal Valley fault, eastern Taiwan. Tectonophysics 333(1–2):199–217. https://doi.org/10.1016/S0040-1951(00)00275-4
Yu SB, Liu CC (1989) Fault creep on the central segment of the longitudinal valley fault, eastern Taiwan. Proc Geol Soc China 32(3):209–231
Yu MS, Cheng SN, Yeh YT (1994) Segmentation of the Taitung longitudinal valley fault zone. Ti-Chih 14(1):97–120
Yu SB, Chen HYC, Kuo LC (1997) Velocity field of GPS stations in the Taiwan area. Tectonophysics 274:41–59

Publisher's Note